

Low-frequency current variability observed at the shelfbreak in the northeastern Gulf of Mexico: May–October, 2004

W.J. Teague*, E. Jarosz, M.R. Carnes, D.A. Mitchell, P.J. Hogan

Naval Research Laboratory, Stennis Space Center, MS 39529-5004, USA

Received 10 November 2005; received in revised form 31 July 2006; accepted 2 August 2006

Available online 2 October 2006

Abstract

High-resolution current measurements were made in the Northeastern Gulf of Mexico by the Naval Research Laboratory (NRL) as part of its Slope to Shelf Energetics and Exchange Dynamics (SEED) project. The major goal of SEED is to understand the mechanisms that transfer properties across the shelf slope. Fourteen acoustic Doppler current profilers (ADCPs) were deployed just west of the DeSoto Canyon on the shelf and down the slope from May to November, 2004 to measure nearly full water column current profiles. Currents were found more variable on the shelf than on the slope but in the mean strongly tended to follow bathymetry, particularly on the slope. During the SEED time period currents were driven by both local and remote winds, by cyclonic eddies associated with the Loop Current extension and Loop Current rings, by smaller eddies associated with the cyclonic eddies, by frontal meanders or streamers associated with the eddies, and by tropical storms. Currents were highly barotropic, accounting for more than 80% of the eddy kinetic energy (EKE). Current magnitudes generally increased from west to east, towards the DeSoto Canyon. Tropical storms had a relatively minor short-term effect upon mass transports. Cross-shelf transports were much smaller than the along-shelf transports. Onshore transports were stronger on the western side of the array while offshore transports were stronger on the eastern side of the array near the DeSoto Canyon. Offshore transports generally occurred during eastward flow periods, onshore transports during westward flow periods, and both during eddy periods. Mesoscale eddies also provided contributions to cross-shelf exchange. Large scale circulation features could be determined from the first two empirical-orthogonal function (EOF) modes which accounted for 83% of the variance and were strongly related to the integrated wind stress.

Published by Elsevier Ltd.

Keywords: Coastal currents; Continental shelf; Continental slope; Barotropic field; Baroclinic field; Gulf of Mexico; (28–31N, 86–90W)

1. Introduction

The continental shelf and slope waters off Mississippi provide a suitable region to study coastal ocean processes. The shelf gently slopes down to

depths of about 100 m off of the Gulf Coast, and then abruptly ends as depths rapidly increase to greater than 1000 m. This region experiences seasonally variable meteorological forcing usually associated with frontal passages. Wind forcing is dominated by cold-front passages during winter and by the Bermuda High during summer while spring and fall are transitional periods (Ford et al., 1988). During fall and winter in the northeastern Gulf of Mexico, winds

*Corresponding author. Tel.: +228 688 4734;
fax: +228 688 5997.

E-mail address: teague@nrlssc.navy.mil (W.J. Teague).

are primarily from the north and are reversed during spring and summer (Gutierrez de Velasco and Winant, 1996). The current flow on the shelf is variable and responsive to wind forcing (Huh et al., 1984). Thermal fronts often form at the shelf break between the shallow shelf waters and adjacent offshore deeper waters (Huh et al., 1978; Garwood et al., 1981). Along the slope, currents generated by the wind flow predominantly in the along-shelf direction. The general flow is eastward but the currents vary significantly on both seasonal and interannual time scales (Hamilton et al., 2000; He and Weisberg, 2002; Hsueh and Golubev, 2002; Wang et al., 2003). Additionally, the region is indirectly affected by the loop current and loop current rings, and directly affected by their associated smaller-scale cyclonic and anticyclonic eddies and frontal meanders (Paluszkie-wicz et al., 1983; Hamilton, 1990; Hamilton et al., 2002; Vukovich, 1988). Interactions of eddies with the shelf water at the shelf break can trigger an exchange of water between the shelf and the deep ocean (Vidal et al., 1992; Ohlmann et al., 2001). Filaments or streamers of warm water from the loop current are not uncommon on the shelf and slope when the loop current extends well into the northeastern Gulf (Hamilton et al., 2000). Shelf and slope exchanges can occur as offshore or onshore jets between eddies rotating in opposite directions. The coastal water mass properties are influenced by freshwater input dominated by the Mississippi River system, which has the largest river discharge in North America.

Currents in the shelf-break region are often more difficult to understand than those on the shelf or in the deep ocean. Coastal processes can force the currents here as well as deep ocean processes, and often both contribute to the forcing. In order to resolve currents along the shelf break and down the slope, high-resolution sampling is needed both vertically, to resolve baroclinic current structures, and horizontally to resolve mesoscale features that may be on the order of just a few tens of kilometers. Additionally, circulation patterns are often determined by the bathymetry, which unfortunately is usually poorly resolved. Bathymetry used in circulation models may not be accurate enough to describe detailed current structures at specific geographic locations. Dynamics in the shelf break region have been difficult to model since the shelf break is usually not well resolved in both coastal and deep ocean models. However, models such as the HYbrid Coordinate Ocean Model (HYCOM) (Chassignet et al., 2006) are being developed to bridge this gap.

To gain a better understanding of the currents in the shelf and slope regime, NRL has undertaken an intensive measurement program as part of its SEED project. With the primary focus on the currents, 14 current moorings consisting of ADCPs and acoustic current meters were deployed on the shelf and down the slope just west of the DeSoto Canyon (Fig. 1). Nearly full water column velocity profiles were measured from moorings on the shelf at water depths less than 100 m, and along the slope at water depths of 500 m. At water depths of 1000 m on the slope, velocity profiles of the upper 500 m, and velocities at about 900 m depth were measured. The purpose of this paper is to describe the low-frequency currents on the shelf and the slope corresponding to periods greater than 40 h for summer and fall of 2004 with emphasis on processes that affect the cross-shelf exchange, and to set the stage for later papers that focus on specific dynamical processes. These observations form one of the best current data sets ever collected that simultaneously encompasses both the shelf and slope region in the Gulf of Mexico.

Section 2 provides a brief description of the data and instrumentation. Basic statistics for the currents are given in Section 3. The shelf and slope currents are described in Section 4 and their depth dependency is discussed in Section 5. Wind forcing is discussed in Section 6. An EOF analysis that addresses the predominant characteristics of the shelf and slope currents is provided in Section 7.

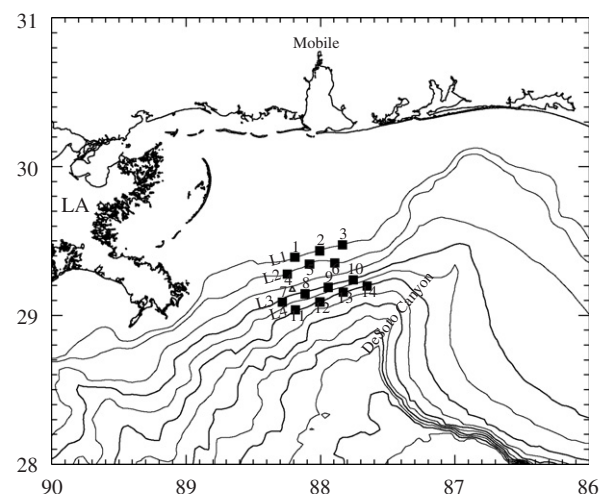


Fig. 1. SEED mooring locations (squares) are shown for lines L1–L4. NDBC buoy 42040 is indicated by the triangle. Contours of bathymetry, increasing offshore, are shown for 60, 90, 250, 500, 750, 1000, 1250, 1500, 1750, 2000, 2250, 2500, and 2750 m.

Discussion and conclusions are presented in Sections 8 and 9, respectively.

2. Data

Fourteen ADCPs were deployed along four lines on the continental shelf and down the slope about 100 miles south of Mobile, Alabama in May 2004 for a one-year deployment. Mooring numbers, bathymetry, and line numbers (L1–L4) are shown in Fig. 1. The moorings were spaced about 10–20 km apart. A midterm servicing of the moorings, after six months of deployment, was performed because of anticipated biological fouling, corrosive processes, and sediment burial of mooring components, particularly on the shelf at shallower depths. These processes can degrade data quality and cause mooring releases to malfunction. Hence, all of the moorings were recovered in November 2004 for refurbishment and data retrieval. Thirteen of the moorings were redeployed at the same locations (M14 was not redeployed due to equipment failure). Final recovery of the moorings was performed in May 2005. The data for the second half of the deployment period (winter and spring) are not discussed here. The moorings survived the passage of Hurricane Ivan, which passed directly over the moorings, however, two of the moorings on

the shelf required recovery by a ROV (remotely operated vehicle) due to extreme mud compaction around the releases attributed to bottom scouring caused by Ivan (Teague et al., 2006). Hurricane Ivan generated currents greater than 2 m/s (Mitchell et al., 2005) and forced huge surface waves over the moorings. One wave measured 27.7 m (91 ft) from crest to trough, and is the largest wave ever directly measured (Wang et al., 2005). Table 1 provides positions, measurement depths, times, water depths, and instrument types for the first half of the deployment period, during summer and fall.

Six of the moorings were deployed on the shelf in trawl-resistant bottom mounts (TRBMs) split evenly in two lines along depth contours of 60 and 90 m (referred to as L1 and L2, respectively). The TRBMs utilized dome-shaped mounting pods, called Barnys because of their barnacle-like shape (Perkins et al., 2000), that are highly resistant to trawling. The Barny mounts were equipped with RD Instruments Workhorse ADCPs operating at 300 kHz, Sea-Bird Electronics Model 26 wave/tide gauges, and EdgeTech acoustic releases for location and recovery. The ADCP heads, situated about 0.5 m off the bottom, recorded current profiles at 2 m resolution every 15 min with an accuracy of 0.5% of the water velocity over nearly the full water column. Inherent to the ADCP design, interference

Table 1
Mooring summary

M	LAT	LON	Start Day	End day	dt	z1	zn	dz	Bottom	TYPE
1	29.39	–88.19	122	305	.25	6	52	2	60	TRBM
2	29.43	–88.01	122	305	.25	4	54	2	60	TRBM
3	29.47	–87.84	122	304	.25	6	54	2	60	TRBM
4	29.28	–88.25	123	304	.25	10	82	2	88	TRBM
5	29.34	–88.08	123	304	.25	11	83	2	89	TRBM
6	29.35	–87.89	123	304	.25	9	81	2	87	TRBM
7	29.09	–88.28	124	311	1.0	52	492	10	515	Long ranger
8	29.14	–88.11	124	312	1.0	52	492	10	518	Long ranger
9	29.19	–87.94	124	312	1.0	50	500	10	518	Long ranger
10	29.24	–87.76	124	312	1.0	51	511	10	518	Long ranger
11	29.04	–88.19	125	312	1.0	53	493	10	1016	Long ranger
					1.0	912				AA RCM9
12	29.09	–88.00	125	312	1.0	53	513	10	1038	Long ranger
					1.0	934				AA RCM9
13	29.16	–87.83	126	312	1.0	50	500	10	1025	Long ranger
					1.0	921				AA RCM9
14	29.20	–87.65	126	312	1.0	52	502	10	1029	Long ranger
					1.0	925				AA RCM9

Columns correspond to Mooring number, Latitude, Longitude, start day and end day in 2004, sampling interval in hours (dt), depths (in m) of top velocity bin (z1) and bottom velocity bin (zn), and bin interval (dz); bottom depth in m, and instrument type (TRBM—trawl resistant bottom mounted 300 kHz ADCP, Long Ranger—75 kHz ADCP, AA RCM9—Aanderraa RCM9 acoustic current meter).

of side lobes with the main lobes of the acoustic beams prevented accurate velocity determinations near the surface (about 5 m at 60 m water depth and 10 m at 90 m water depth). Water temperatures were recorded with a resolution of 0.01°C . The data from the Sea-Bird Electronics wave and tide gauges will not be discussed here but have been reported on by Wang et al. (2005) pertaining to a study of storm waves generated by Hurricane Ivan.

The other eight moorings were deployed down the continental slope. Each of these moorings contained an RD Instruments Long Ranger ADCP operating at 75 kHz mounted in a Flotation Technology buoy, 45-in in diameter. Two lines consisting of four moorings each were deployed along the 500 and 1000 m depth contours (referred to as L3 and L4), respectively. Upper water column current profiles from approximately 500 to 50 m below the surface were measured every hour at 10 m resolution with an accuracy of $\pm 1\%$ of the water velocity. Additionally, at the deep moorings along L4, an Aanderaa RCM9 Doppler current meter was located about 100 m off the bottom near 900 m depth and recorded current speed, current direction, temperature, and pressure. Accuracies of the corresponding velocities were well under 1 cm/s.

The data records were complete and very little editing was required for the recorded data. High-frequency currents not of concern here, such as tides and inertial currents, were removed from the current records by applying a low-pass filter with a 40-h cutoff frequency. Currents at the shelf break and along the continental slope were bathymetrically steered. The bathymetric contours are approximately parallel and are tilted about 20° counter-clockwise from an east to west line (Fig. 1). For some of the analyses performed here, the current data were rotated 20° clockwise so that u components are along shelf and v components are across shelf. Positive u values, generally eastward, will be referred to as upcoast and negative u values will be referred to as downcoast. Positive v values, generally northward, and negative v values, generally southward, will be referred to as onshore and offshore, respectively.

3. Statistics

The ADCP data provided excellent vertical resolution for examining the shelf and slope processes, ranging from 2 m resolution on the shelf to 10 m resolution on the slope (Table 1). Basic

statistics for each mooring over the May–October period for the low-pass filtered and rotated data for the top, several mid-level, and bottom velocity bins are given in Table 2. The standard error listed here is defined as the standard deviation divided by the square root of the number of degrees of freedom, which is estimated as the sample period divided by the integral time scale. The integral time scale is defined as the discrete integral of the time-lagged autocorrelation function from zero lag to the first zero crossing after demeaning and detrending the time series. Integral time scales ranged from approximately 2 to 30 days, with longer time scales found in the along shelf component over the slope. Integral time scales on the shelf were generally about a week or less and could be related to local wind events. Time scales of velocities along the slope were about a month and appeared to have been lengthened, compared to scales on the shelf, by the effects of a strong seasonal cycle (Fig. 2a). Close examination of the along shelf velocity time series over the slope revealed two disparate time scales of about a week and about three months. Combination of the two time scales produced an integral time scale of about a month. A single integral time scale is not adequate to define scales of motion when two markedly different time scales are present. Shorter time scales of about a week were found near the bottom along the slope, similar to scales on the shelf, and apparently result from a reduction of the seasonal cycle near the bottom. These integral time scales observed in the Gulf of Mexico are similar to those that have been observed in the Atlantic where time scales are shorter near boundaries and longer in the ocean interior (Hogg et al., 1999).

From individual mooring statistics over the measurement period of May–October 2004, the maximum upcoast mean current velocity was about 11 cm/s (M14 at 100 m) and the maximum mean downcoast current velocity was about 5 cm/s (M9 at 500 m). The maximum mean onshore current velocity was nearly 3 cm/s (M11 at 53 m) and the maximum mean offshore velocity was about 3 cm/s (M4 at 82 m and M10 at 101 m). The largest along slope velocities were usually directed downcoast. On the shelf, the maximum upcoast velocity, 56 cm/s, was found near the surface at M5 while the maximum downcoast velocity was 87 cm/s at M1 near the surface. On the slope, the maximum downcoast velocity, 89 cm/s, was found at 300 m depth at M10 while the largest upcoast velocity was 48 cm/s at 53 m depth at M11. The largest

Table 2

Basic statistics over the entire measurements period for selected depth levels

	Z	\bar{U}	σ_u	SE_u	U_{\min}	U_{\max}	\bar{V}	σ_v	SE_v	V_{\min}	V_{\max}	Spd_{\max}	Dir_{\max}	IT_u	IT_v	MKE	EKE
M1	6	2.44	12.77	2.94	−87.28	38.52	0.95	12.27	1.71	−34.41	64.06	90.93	286.31	9.55	3.50	3.42	156.79
M1	30	0.01	9.67	1.74	−78.59	26.25	0.37	7.73	1.16	−21.51	53.71	84.53	292.40	5.80	4.05	0.07	76.63
M1	52	−2.69	6.77	1.09	−52.89	14.09	−1.28	4.91	0.45	−30.74	31.79	52.97	273.74	4.64	1.48	4.45	34.98
M2	4	3.42	14.85	3.49	−65.12	41.28	0.16	12.39	1.71	−31.92	47.71	69.85	291.47	9.90	3.41	5.85	186.99
M2	30	1.50	11.18	1.81	−63.76	48.67	−1.44	8.17	1.08	−30.83	33.82	71.59	297.20	4.68	3.11	2.16	95.87
M2	54	−0.80	9.34	1.41	−48.22	30.90	−2.30	5.07	0.60	−52.40	13.10	54.00	196.24	4.06	2.49	2.95	56.45
M3	6	3.72	14.05	3.12	−54.32	33.20	−0.25	10.22	1.46	−29.39	34.60	63.81	302.00	8.79	3.65	6.96	150.84
M3	30	1.85	11.61	1.83	−50.01	42.17	−1.12	6.99	0.88	−27.96	38.93	63.38	307.90	4.45	2.81	2.34	91.86
M3	52	−1.36	9.51	1.41	−45.58	36.47	−0.92	3.62	0.39	−23.25	13.09	46.00	262.10	3.92	2.10	1.34	51.73
M4	10	2.91	18.69	6.97	−66.57	49.06	0.02	9.64	1.67	−28.98	36.20	70.42	291.89	24.78	5.34	4.24	221.18
M4	30	4.45	14.76	4.82	−71.05	40.27	−0.20	7.58	1.35	−22.75	48.82	78.56	295.32	18.98	5.61	9.92	137.59
M4	50	2.75	13.02	2.54	−65.04	36.42	−0.79	6.29	0.93	−19.77	52.28	75.40	307.50	6.80	3.90	4.10	104.54
M4	82	1.06	12.02	1.98	−58.96	34.92	−2.73	4.31	0.82	−33.41	9.08	58.99	268.05	4.83	6.47	4.30	81.56
M5	11	4.65	16.29	5.56	−60.25	56.18	0.55	10.11	1.57	−29.71	50.27	71.86	303.90	20.72	4.27	10.96	183.74
M5	31	3.60	12.81	2.46	−61.67	56.02	0.44	7.41	1.07	−18.55	43.37	74.07	303.66	6.57	3.67	6.59	109.51
M5	51	3.21	12.64	2.34	−59.56	50.99	−0.29	5.47	0.63	−14.20	57.61	74.64	316.66	6.08	2.39	5.18	94.86
M5	83	−1.49	8.41	1.32	−50.45	19.92	−0.66	3.82	0.37	−47.62	15.67	55.01	210.10	4.40	1.63	1.32	42.67
M6	9	5.17	16.82	5.33	−61.07	43.82	−0.37	9.31	1.33	−28.40	44.33	70.77	300.34	17.82	3.59	13.42	184.81
M6	31	6.28	14.14	2.93	−47.22	38.62	−1.30	6.19	0.85	−17.72	42.51	58.23	316.89	7.60	3.34	20.54	119.20
M6	51	5.46	14.09	2.60	−44.32	38.81	−1.57	5.81	0.83	−22.13	33.45	54.40	306.42	6.02	3.64	16.13	116.19
M6	81	−0.15	10.09	1.80	−45.10	28.51	−1.39	5.17	0.81	−41.43	8.57	52.30	217.69	5.62	4.36	0.97	64.26
M7	52	2.38	19.09	7.51	−63.96	41.92	1.72	5.46	0.81	−17.59	29.21	66.77	290.24	28.47	4.02	4.30	197.07
M7	102	2.65	17.40	6.92	−52.93	27.68	0.42	4.65	0.68	−16.31	25.71	53.18	276.45	29.10	3.92	3.61	162.07
M7	202	0.38	16.73	6.22	−69.91	28.12	0.33	3.21	0.37	−15.20	12.87	69.98	272.59	25.39	2.47	0.13	145.07
M7	302	−2.54	15.15	5.46	−73.11	21.68	0.02	2.30	0.27	−13.21	6.13	73.11	270.07	23.82	2.49	3.22	117.44
M7	492	−4.08	10.67	2.19	−51.99	27.01	−0.88	1.98	0.29	−9.93	4.75	52.54	261.74	7.74	3.96	8.71	58.86
M8	52	4.55	19.50	7.60	−72.39	36.42	1.48	5.35	1.04	−17.88	38.95	81.66	297.90	28.10	6.98	11.45	204.42
M8	102	5.69	19.22	7.42	−57.44	30.72	0.51	4.18	0.76	−13.62	21.00	57.77	277.27	27.57	6.09	16.31	193.39
M8	202	1.59	18.22	6.68	−77.18	28.93	0.20	2.92	0.37	−11.80	16.96	77.24	267.64	24.83	3.02	1.29	170.14
M8	302	−2.06	16.48	5.65	−74.47	27.43	0.21	2.16	0.32	−8.90	9.30	74.48	270.77	21.70	4.04	2.14	138.05
M8	492	−1.59	11.33	2.31	−58.74	30.41	−0.14	1.72	0.24	−7.87	6.64	58.81	267.37	7.69	3.66	1.28	65.63
M9	50	6.21	19.45	7.42	−77.76	41.33	0.44	5.85	1.37	−17.46	33.85	84.41	293.24	26.87	10.19	19.40	206.18
M9	100	7.31	19.61	7.25	−67.84	40.65	−0.27	5.41	1.13	−13.73	42.60	75.71	298.66	25.21	8.01	26.74	206.95
M9	200	2.16	18.97	6.72	−82.42	30.63	−0.22	3.47	0.94	−14.32	15.18	83.63	279.75	23.20	13.61	2.36	185.99
M9	300	−2.04	17.63	5.96	−77.16	24.95	0.34	3.07	0.90	−6.65	13.32	78.20	279.38	21.12	15.93	2.14	160.12
M9	500	−4.82	11.42	2.10	−53.47	25.32	0.19	1.03	0.09	−7.96	4.67	53.47	269.55	6.22	1.47	11.64	65.69
M10	51	8.37	18.32	6.51	−64.81	40.10	−2.51	6.47	1.56	−21.58	33.44	64.82	268.82	23.29	10.73	38.15	188.69
M10	101	8.43	20.30	7.30	−69.53	45.53	−2.97	6.41	1.71	−24.32	34.39	75.54	294.50	23.85	13.18	39.95	226.55
M10	201	1.70	20.81	7.13	−86.28	36.59	−2.12	4.40	1.49	−14.83	10.35	86.40	273.09	21.69	21.31	3.68	226.13
M10	301	−4.04	18.40	5.65	−88.91	26.69	−0.84	2.84	0.76	−9.66	9.34	89.05	273.26	17.37	13.24	8.51	173.36
M10	511	−3.38	9.74	1.66	−45.60	34.97	−1.04	1.45	0.14	−5.72	5.21	45.66	267.16	5.38	1.70	6.24	48.48
M11	53	3.14	18.24	7.36	−53.32	48.20	3.18	5.65	0.87	−19.64	35.41	58.84	303.39	29.93	4.40	9.97	182.22
M11	103	3.43	15.29	6.36	−39.57	32.32	2.01	4.49	0.67	−17.11	24.35	40.90	255.32	31.78	4.14	7.90	126.98
M11	203	1.46	13.26	5.35	−38.16	31.15	1.28	3.13	0.46	−16.07	15.41	40.11	249.66	29.85	3.95	1.89	92.84
M11	303	−0.76	11.53	4.31	−41.28	17.85	0.86	2.56	0.33	−13.64	11.45	41.49	264.19	25.72	3.04	0.65	69.75
M11	493	−2.95	9.94	3.00	−41.81	17.94	0.43	1.99	0.28	−6.39	9.83	41.91	266.12	16.76	3.57	4.46	51.34
M11	900	−1.76	4.81	0.70	−18.74	9.55	−0.31	1.84	0.19	−7.90	6.10	19.10	257.63	3.91	1.93	1.60	13.26
M12	53	5.60	18.05	7.34	−55.90	43.01	2.10	5.93	1.25	−17.26	35.85	65.27	301.53	30.32	8.11	17.90	180.38
M12	103	6.05	15.51	6.32	−36.33	35.51	1.38	4.58	1.01	−11.16	26.20	38.49	296.83	30.50	8.88	19.24	130.68
M12	203	3.64	13.68	5.26	−37.34	32.29	0.59	3.25	0.59	−13.08	16.38	37.76	250.35	27.06	6.07	6.81	98.87

Table 2 (continued)

	Z	\bar{U}	σ_u	SE_u	U_{\min}	U_{\max}	\bar{V}	σ_v	SE_v	V_{\min}	V_{\max}	Spd_{\max}	Dir_{\max}	IT_u	IT_v	MKE	EKE
M12	303	0.64	12.23	4.34	−43.58	19.76	0.64	2.60	0.49	−8.97	12.15	43.75	275.07	23.10	6.43	0.41	78.08
M12	513	−2.05	10.70	3.03	−42.89	19.06	0.08	2.26	0.34	−7.82	8.71	42.90	270.69	14.69	4.24	2.11	59.78
M12	900	−1.46	7.41	1.24	−22.46	17.39	−0.08	1.33	0.18	−5.05	4.13	22.68	261.95	5.16	3.50	1.06	28.30
M13	50	7.54	18.63	6.98	−86.87	41.60	−0.16	6.41	1.77	−22.88	37.19	88.19	279.98	25.63	13.99	28.44	193.98
M13	100	7.98	16.37	6.47	−55.83	34.16	−0.71	6.00	1.62	−16.09	39.42	61.84	299.29	28.55	13.27	32.12	151.91
M13	200	4.55	15.64	5.70	−54.41	28.62	−1.53	4.30	0.96	−15.10	16.32	54.48	267.02	24.25	9.08	11.54	131.47
M13	300	0.71	14.16	4.70	−55.52	21.16	−1.01	3.40	0.77	−13.91	12.24	55.57	272.58	20.10	9.44	0.76	106.00
M13	500	−1.70	12.06	2.88	−47.75	28.48	−0.13	1.93	0.27	−5.97	7.62	47.79	272.28	10.41	3.52	1.46	74.52
M13	900	−1.71	7.58	1.23	−24.10	21.02	0.24	1.11	0.10	−3.94	6.32	24.30	277.41	4.84	1.60	1.49	29.32
M14	52	10.29	17.04	5.98	−64.11	46.38	−1.38	6.36	2.18	−19.37	22.23	64.41	264.45	22.48	21.40	53.86	165.40
M14	102	10.58	16.26	6.02	−61.82	35.72	−1.93	6.88	2.02	−23.25	23.32	62.84	282.16	25.01	15.78	57.84	155.87
M14	202	5.24	15.46	5.57	−54.62	30.03	−1.96	6.31	1.38	−25.85	23.15	54.62	269.93	23.65	8.74	15.64	139.31
M14	302	1.33	13.57	4.28	−55.30	23.74	−1.06	4.05	0.91	−13.60	12.92	55.39	273.19	18.15	9.14	1.44	100.31
M14	502	−1.53	11.66	2.59	−46.21	32.20	−0.20	2.85	0.49	−18.48	7.05	46.25	272.32	8.98	5.34	1.19	72.00
M14	900	−1.33	7.30	1.27	−25.34	19.78	0.11	1.53	0.19	−10.10	5.90	25.40	266.10	5.55	2.93	0.89	27.83

Current components u and v have been rotated 20° clockwise so that they are approximately parallel and normal to bathymetry contours, respectively. Columns correspond to mooring M, measurement depth Z, average current component \bar{U} , standard deviation σ_u , standard errors SE_u , minimum u value U_{\min} , maximum u value U_{\max} , and similarly for v , maximum speed Spd_{\max} , direction of the maximum speed Dir_{\max} , integral time scales IT_u and IT_v , mean kinetic energy MKE and mean eddy kinetic energy EKE. Units are cgs.

cross-shelf velocities were generally onshore. On the shelf, the maximum onshore velocity was 64 cm/s at M1 near the surface while the largest offshore velocity was 52 cm/s at M2 near the bottom. On the slope in the upper 500 m, the largest onshore velocity was 43 cm/s at M9 at 100 m while the largest offshore velocity was 26 cm/s at M14 at 202 m depth. The largest maximum current speed of 91 cm/s was observed at M1 at 10 m depth and the smallest maximum current speed of 38 cm/s was observed at M12 at 203 m depth. Maximum current speeds at 900 m ranged from 19 to 25 cm/s. Large currents recorded during Hurricane Ivan were filtered out by the 40-h low-pass filter but the maximum observed unfiltered current during Hurricane Ivan was 225 cm/s.

Currents were commonly stronger at depth than closer to the surface, and magnitudes often increased towards the bottom. On the shelf, currents exceeding 90 cm/s were found near the surface and currents exceeding 50 cm/s were found just off the bottom. On the slope at water depths of about 500 m, maximum current velocities, exceeding 70 cm/s, were found between 200 and 300 m in depth, while at the 1000 m mooring sites currents ranged between 38 and 56 cm/s between 200 and 300 m and were maximum closer to the surface.

Currents at 900 m depth, about 100 m above the bottom, displayed similar trends to currents found

at 500 m Downcoast flows were dominant and the mean values over the measurement period were smaller than at 500 m except at M13, where the mean value was about the same as at 500 m. Variance at 900 m was about 25% less than the variance at 500 m. Mean flow in the cross-shelf direction at 900 m was less than 1 cm/s, but was onshore at M13 and M14 and offshore at M11 and M12, opposite to the mean flow at 500 m.

Eddy kinetic energy (EKE) on the shelf ranged from a low of about $35 \text{ cm}^2/\text{s}^2$ near the bottom at M1 to $221 \text{ cm}^2/\text{s}^2$ near the surface at M4. EKE on the slope ranged from $13 \text{ cm}^2/\text{s}^2$ at 900 m depth at M11 to $226 \text{ cm}^2/\text{s}^2$ at 100 m depth at M10. Mean kinetic energy generally ranged from 1 to 50 of cm^2/s^2 . EKE was dominant due to the weak mean flows. EKEs computed here were generally about 50% larger than EKEs extracted from velocity variance ellipses computed using altimeter-derived velocities and drifter-derived velocities just west of the DeSoto Canyon (Ohlmann et al., 2001).

4. Currents

The currents in the SEED region are dominated by the along-shelf component. Maps of the rotated current components as a function of depth and time are shown for each of the moorings in Fig. 2. Time-averaged profiles of velocity for each of the four lines

are shown in Fig. 3. Four time periods are identified by the contrasting current structures, most clearly observed in the u components of velocity (Fig. 2a, Fig. 3). During time period 1 (P1, May), a strong downcoast current dominated the flow, and was particularly evident at the deeper moorings along L3 and L4. June was designated as a transition period (P2) where the currents switched from downcoast to upcoast. Strong upcoast flow was present in July and August (P3). Highly variable currents, particularly on the shelf (L1 and L2) dominated during September and October (P4). Offshore flow was more frequently associated with upcoast flows as can be seen by occurrences of negative v velocity components from July through September (Fig. 2b). However some offshore flow was found with downcoast flows, such as in October.

During P1, the largest average downcoast currents, about 28 cm/s, occurred while the corresponding cross-shelf currents were almost entirely onshore at a few cm/s (Fig. 3). During P2, along-shelf currents were dominant and progressively increased in magnitude from west to east (upcoast). Upcoast currents dominated on the shelf in the upper water column while downcoast currents dominated the lower water column. Upcoast currents were progressively stronger towards the east on the slope with depth. Cross-shelf currents of just a few cm/s were mostly offshore on L1, mixed on L2, and generally onshore at a few cm/s at L3 and L4. During P3, the largest upcoast currents, about 25 cm/s, and largest offshore currents, about 8 cm/s, were found; current velocities generally decreased with depth. During P4, two-layer along-shelf flow patterns were found.

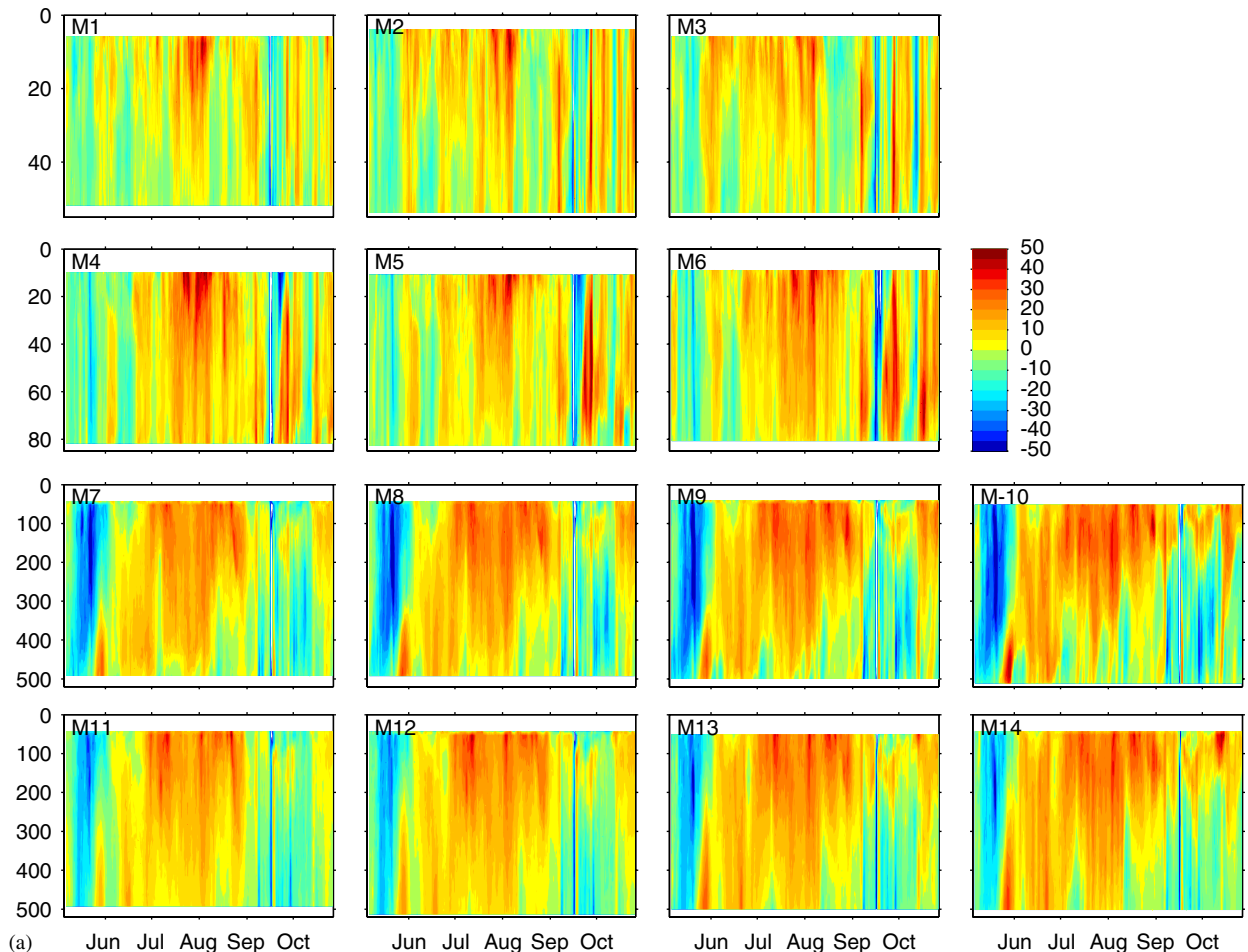


Fig. 2. (a) Velocity time series for the u or along-shelf component; (b) velocity time series for the v or cross shelf component. Velocities (cm/s) have been rotated 20° clockwise so that u and v velocity components are approximately parallel and normal to bathymetry contours, respectively. Tides have been removed using a low-pass filter with a 40-h cutoff frequency.

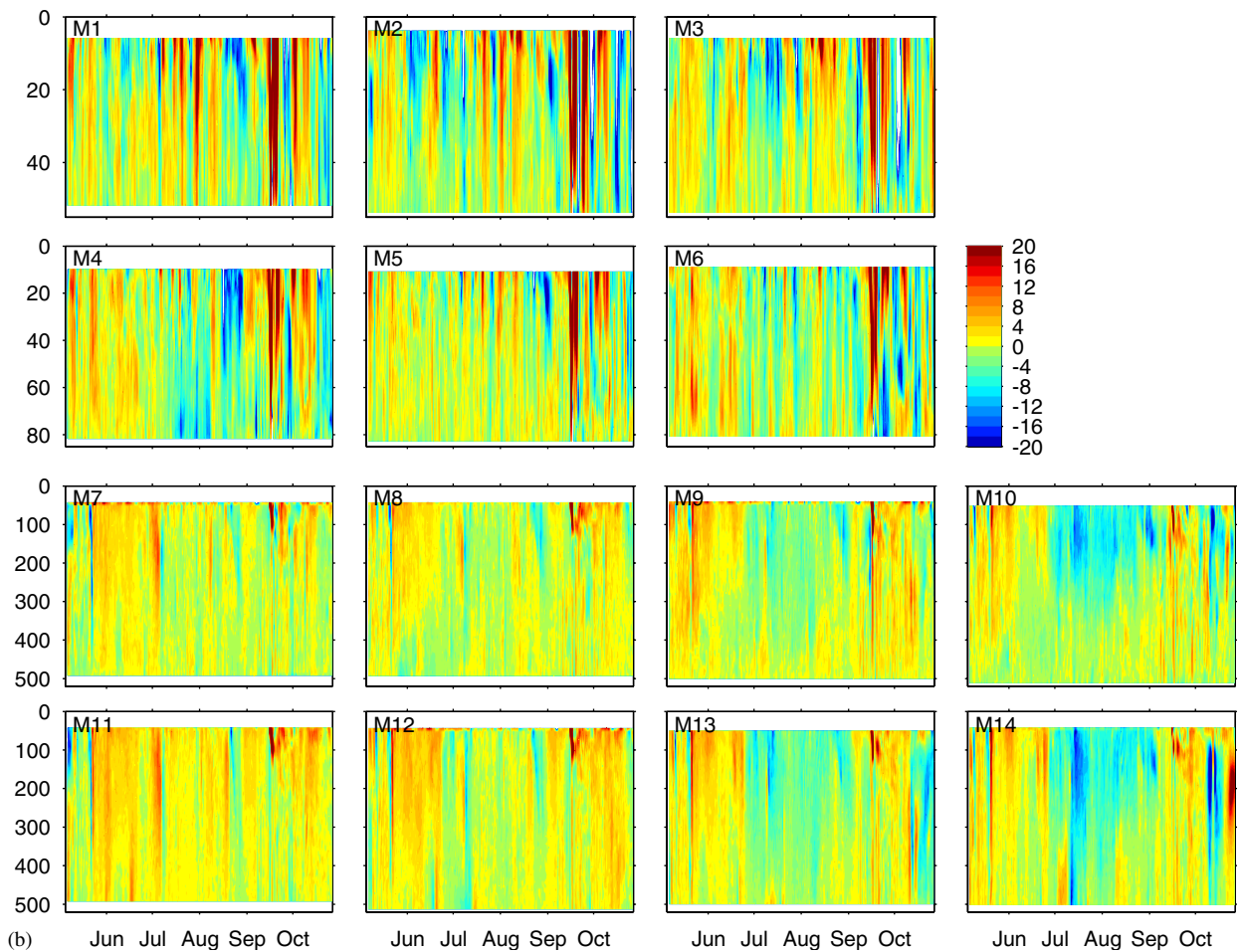


Fig. 2. (Continued)

Upcoast currents increased from west to east on the shelf and in the upper 150 m on the slope. Cross-shelf flows were small and mainly onshore on the slope. Cross-shelf flows on the shelf were mainly onshore in the upper water column and offshore in the lower water column.

Coherences in currents between the moorings and between the surface and mid-depths were high. Currents at 900 m (not shown) were similar in magnitude and direction to the currents at 500 m during the eddy periods (P1 and P4). During the upcoast flow period (P2 and P3), flow at 900 m was small and generally did not compare well with the flow at 500 m. Intense currents on September 15, 2004 (day 260, Fig. 2) was associated with the passage of Hurricane Ivan which passed over the moorings in less than one day. The impact of the hurricane was also evident in the currents at 900 m.

Mean currents closely followed the bathymetry, particularly for the deeper moorings (L3 and L4), and hence were bidirectional, either upcoast or downcoast much of the time. A geographical picture of the mean current field is shown by mapping the vertically averaged currents at each of the moorings over each of the four time periods with standard deviation ellipses (Fig. 4). The center of the standard deviation ellipse is at the tip of the arrowhead and reflects the area that is within one standard deviation of the mean. The stronger mean currents, and best determined currents, occurred during P1–P3 along L3 and L4, and during P3 along L2, and had means larger than their respective deviation ellipses. High variability, indicated by the major axes of the standard deviation ellipses, generally appeared in the direction of the mean flows and along bathymetry contours for L2–L4. Higher variability occurred

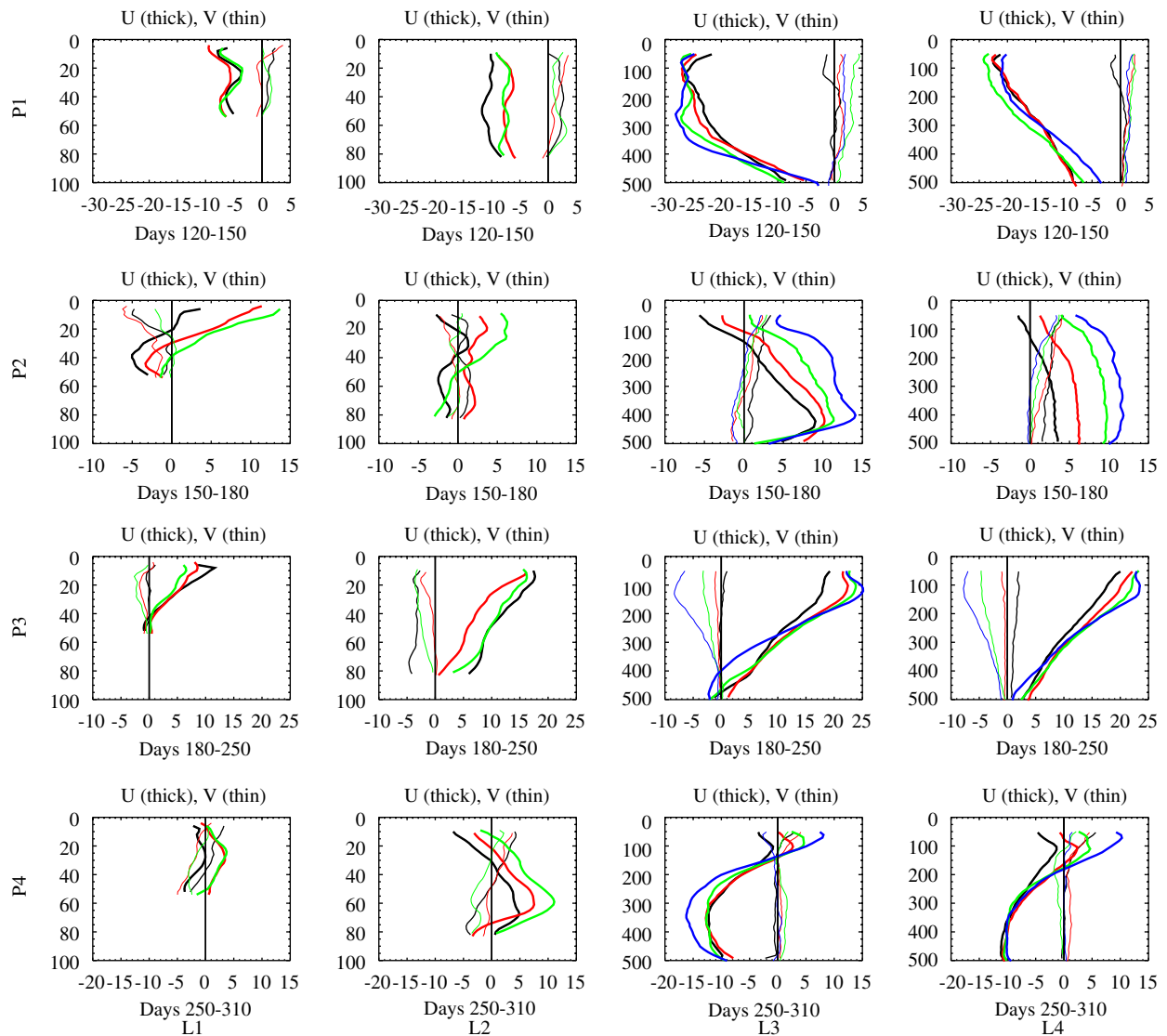


Fig. 3. Time-averaged velocity profiles (cm/s) over depth for four different time periods are shown for each of the four mooring lines. Time periods are: P1, year days 120–150 (May); P2, 150–180 (June); P3, 180–250 (July to August); and P4, 250–310 (September to October). Lines are: L1–M1, M2, and M3; L2–M4, M5, and M6; L3–M7, M8, M9, and M10; and L4–M11, M12, M13, and M14. Black, red, green, and blue colors correspond to moorings from west to east along each line. Thick lines correspond to along-shelf (u) components and thin lines correspond to cross-shelf (v) components. Positive u values are upcoast and positive v values are onshore.

on the shelf along L1 and L2 and was highest during P4. On the shelf along L2, significant mean downcoast flows occurred during P1 (M4 and M5) while significant mean upcoast flows occurred during P3. Onshore flow was apparent along L3 and L4 during P2 while offshore flow was suggested during both upcoast and downcoast flows along L3 and L4 on the eastern side of the array during P3 and P4, respectively. Some onshore flow was found on the

western end of L4 during upcoast and downcoast flows in P3 and P4, respectively.

Progressive vector diagrams for each of the moorings further illustrate the vertically averaged mean flow conditions over the measurement period (Fig. 5). The vector diagrams, originating at the mooring locations marked by squares first indicated downcoast currents, then upcoast currents, and finally downcoast currents again with some eddy

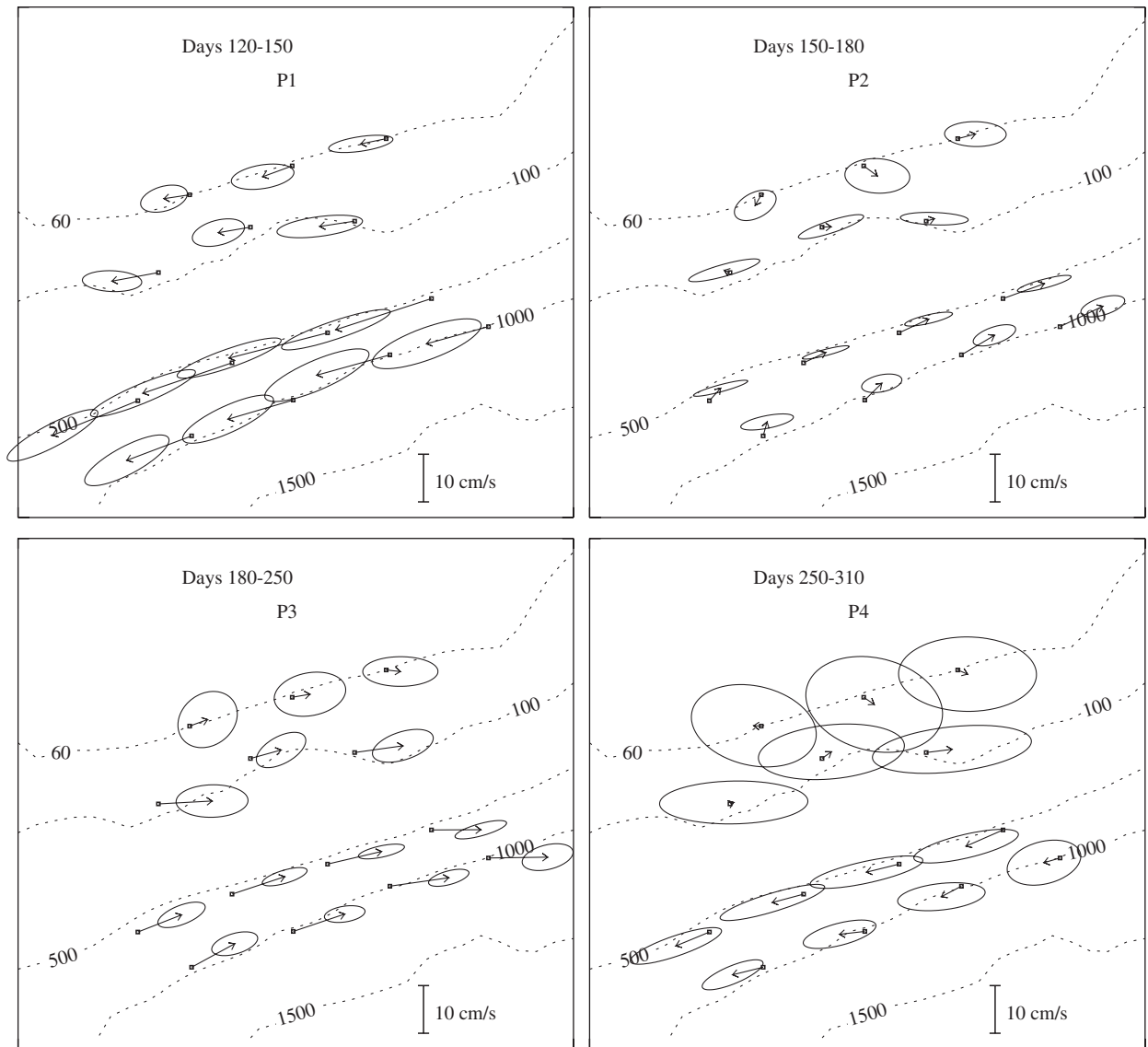


Fig. 4. Mean currents (cm/s) and their corresponding standard deviation ellipses after tide removal are shown at each of the mooring sites for the four time periods described in Fig. 3.

variability near the end of the measurement period for L3 and L4. Similar conditions were found on L2 with higher eddy variability occurring near the end of the measurement period. High eddy variability was observed on L1, with the highest eddy variability at M1. The net vector (the vector connecting starting point to ending point), suggestive of water mass movement, was negligible at M1 and southeastward at M2 and M3 along L1; eastward at M4 and M6, and northeastward at M5 along L2; negligible at M7, northeastward at M8 and M9, and southward at M10 along L3; north-

ward at M11, northeastward at M12, and eastward at M13 and M14 along L4. Net vectors suggested offshore water movement on the eastern ends of L3 at M10 and L4 at M13 and M14, and onshore water movement on the western end of L4 at M11 and M12. Water movement was closely aligned with the 500 m contour at M7, M8, and M9 along L3. There was a pulse of onshore flow when the flow direction turned rapidly from downcoast to upcoast and a pulse of offshore flow when the flow direction turned from upcoast to downcoast. Currents, particularly at the deep moorings (L3 and L4), nearly followed the

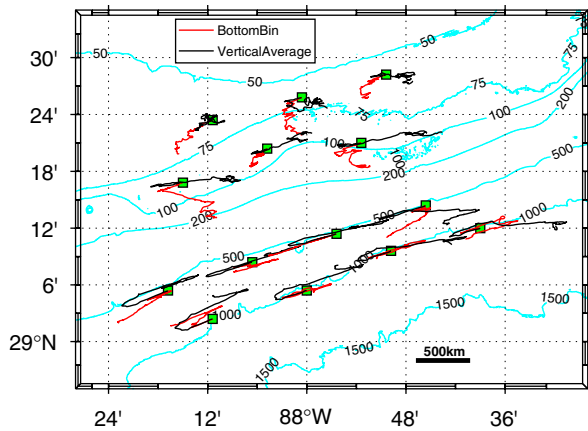


Fig. 5. Progressive vector diagrams for the vertically averaged currents (black) and the bottom velocity bin (red) are shown at each of the mooring sites. The vector scale is provided in the lower right corner. Contours of bathymetry in m are shown in green.

along-shelf bathymetry contours. Progressive vector diagrams are also shown for the deepest measured velocities (bottom bin) in Fig. 5. Offshore near-bottom flow was observed at all of the shelf moorings (L1 and L2) while on the slope the bottom-bin velocities were similar to the vertically averaged velocities, but slower.

The depth-averaged rotated u and v velocities at each of the moorings are indicative of the relative magnitudes of the along- and cross-shelf transports, respectively (Fig. 6). The along-shelf velocities (u) were fairly consistent between moorings on each line. Velocities on the slope were generally down-coast at the beginning and end of the measurement period and upcoast during the middle period (Fig. 6a). The cross-shelf velocities (v) (Fig. 6b) were much smaller than the along-shelf velocities and more variable between moorings on each line. Both on

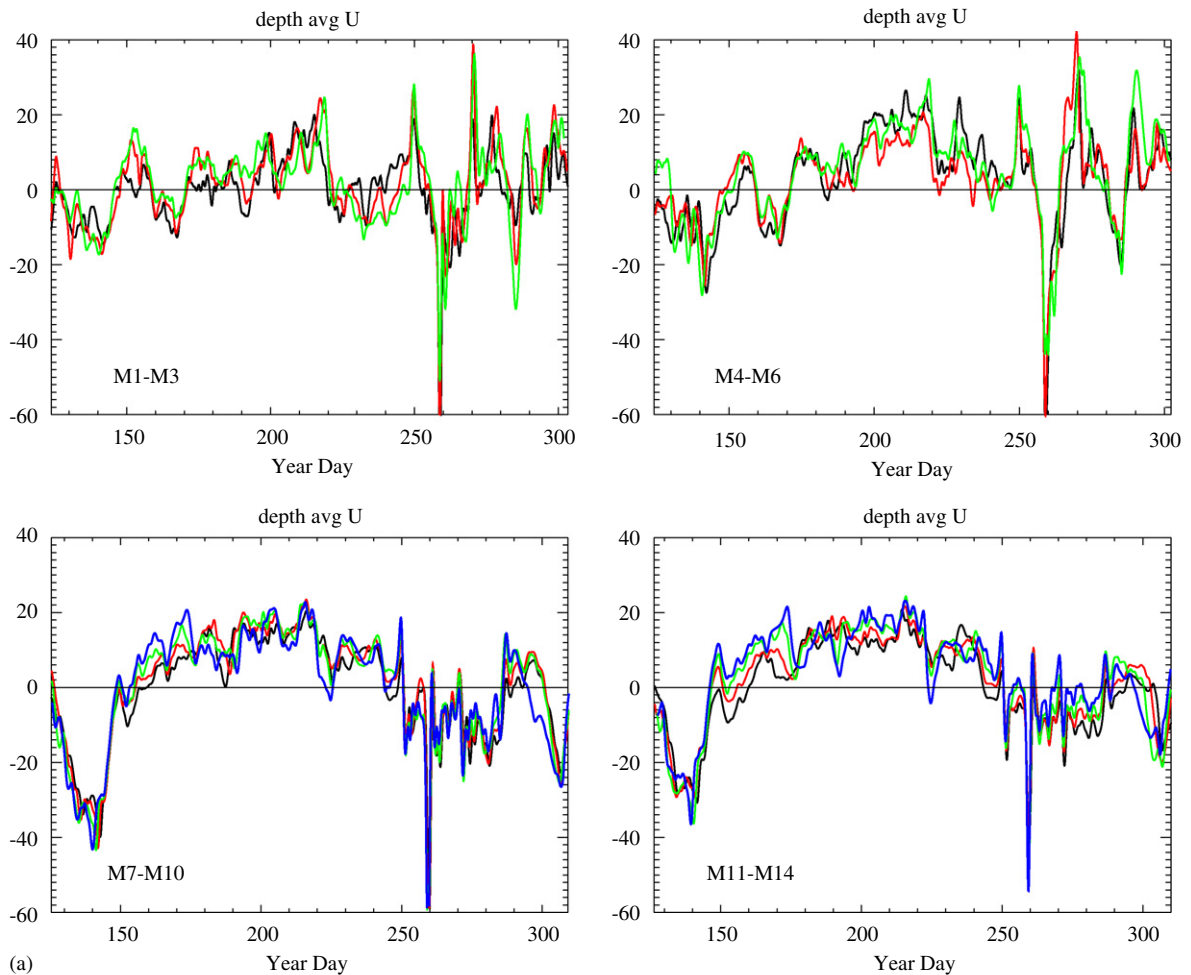


Fig. 6. Depth averaged velocity time series (cm/s) are shown for the four time periods and four lines (described in Fig. 4). Black, red, green, and blue colors correspond to moorings from west to east along each line: (a) along-shelf component (u); (b) cross-shelf component (v).

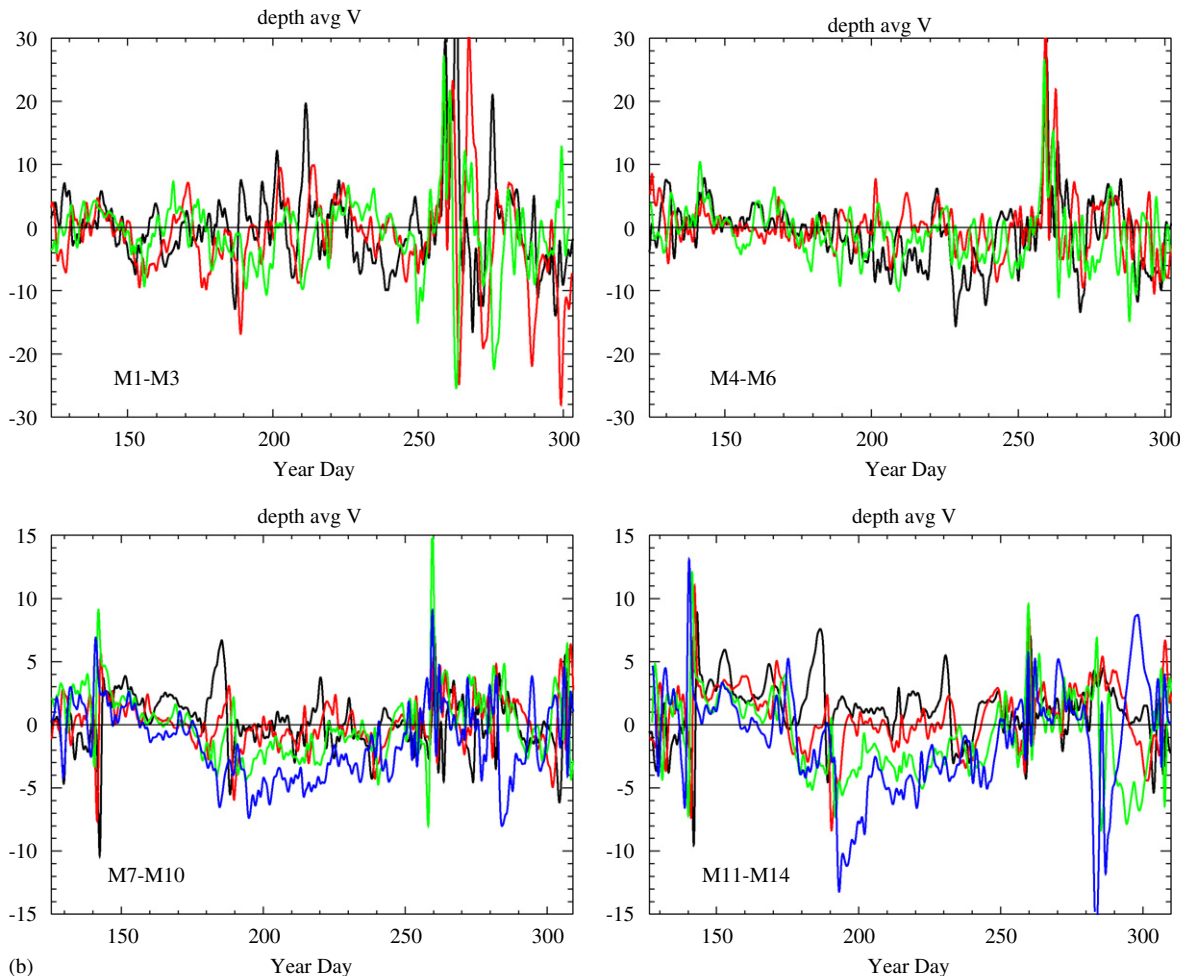


Fig. 6. (Continued)

and offshore currents are associated with the meso-scale eddy activity that occurred at each end of the record (P1 and P4). Several periods of clear cross-shelf transport are indicated (Fig. 6b). Large onshore and offshore flows were observed near day 260 (Hurricane Ivan) on all four lines, and near days 140 and 285 on L3 and L4. Offshore flow was found between days 180 to 250 at the two eastern-most mooring on L3 and L4. One of the strongest offshore flows (13 cm/s) occurred at M14 near day 190 and was about twice as large as the offshore flows at the other moorings on L4.

Short-term variability in the velocity data makes identification of long-term trends in the transports difficult. Cumulative time integrals of the transports minimize the short-term variability in comparison to the long-term trends. Cumulative volume transported

(CVT) per unit width versus time at each of the moorings is examined by integrating the depth-averaged velocities from the beginning of the measurement period up to each time in the measurement period and multiplying by water depth for lines L1–L3, and by 500 m for line L4. CVT provides a comparison of the total volume transported at each mooring along the four lines. CVT for the along-shelf and cross-shelf components of velocity versus time are shown in Figs. 7a and b, respectively. Positive (negative) slopes in CVT are due longer term trends in upcoast (downcoast) and onshore (offshore) transports. The along-shelf CVT (Fig. 7a) displays similar overall trends among moorings on each line. From the beginning of the observation period to about day 150, CVT decreases due to a long-term downcoast transport. Between days 150 and 250, CVT increases

due to a long-term upcoast transport. For the remainder of the measurement period, CVT increases on L2 due to long-term upcoast transport, remains nearly constant on L1, and decreases on L3 and L4 due to long-term downcoast transport. Along L4, CVT progressively increases from west to east, indicating larger upcoast transport near the DeSoto Canyon. On all four lines, CVT is smaller on the western side. Cross-shelf CVT is quite different among moorings on each of the lines (Fig. 7b). CVT increases at the beginning of the measurement period on all four lines due to long-term onshore transport. Then, over the slope, CVT remains nearly constant at M7–M9 along L3 with very little cross-shelf transport but CVT decreases at M10 due to offshore transport. On L4, CVT increases at M11 and M12 due to onshore transport and decreases at M13

and M14 due to offshore transport. On the shelf, CVT generally decreases at M2 and M3 on L1 and at M4 and M6 on L2, due to offshore transport. CVT fluctuates, without an overall trend, at M1 on L1 and M5 on L2, suggesting little long-term cross-shelf transport. Therefore, on the slope, CVT indicates that transport was generally onshore on the western side of the moorings and offshore on the eastern side, closest to the DeSoto Canyon. CVT over the entire SEED measurements period (up to day 310) was larger when offshore than when onshore along L1–L3, but magnitudes of onshore (M11, M12) and offshore (M13, M14) CVT were similar along L4. Cross-shelf transports were smaller on the shelf than on the slope by about a factor of 10. Hurricane Ivan effects (near day 260) on CVT were small because of its relatively short duration compared to the total

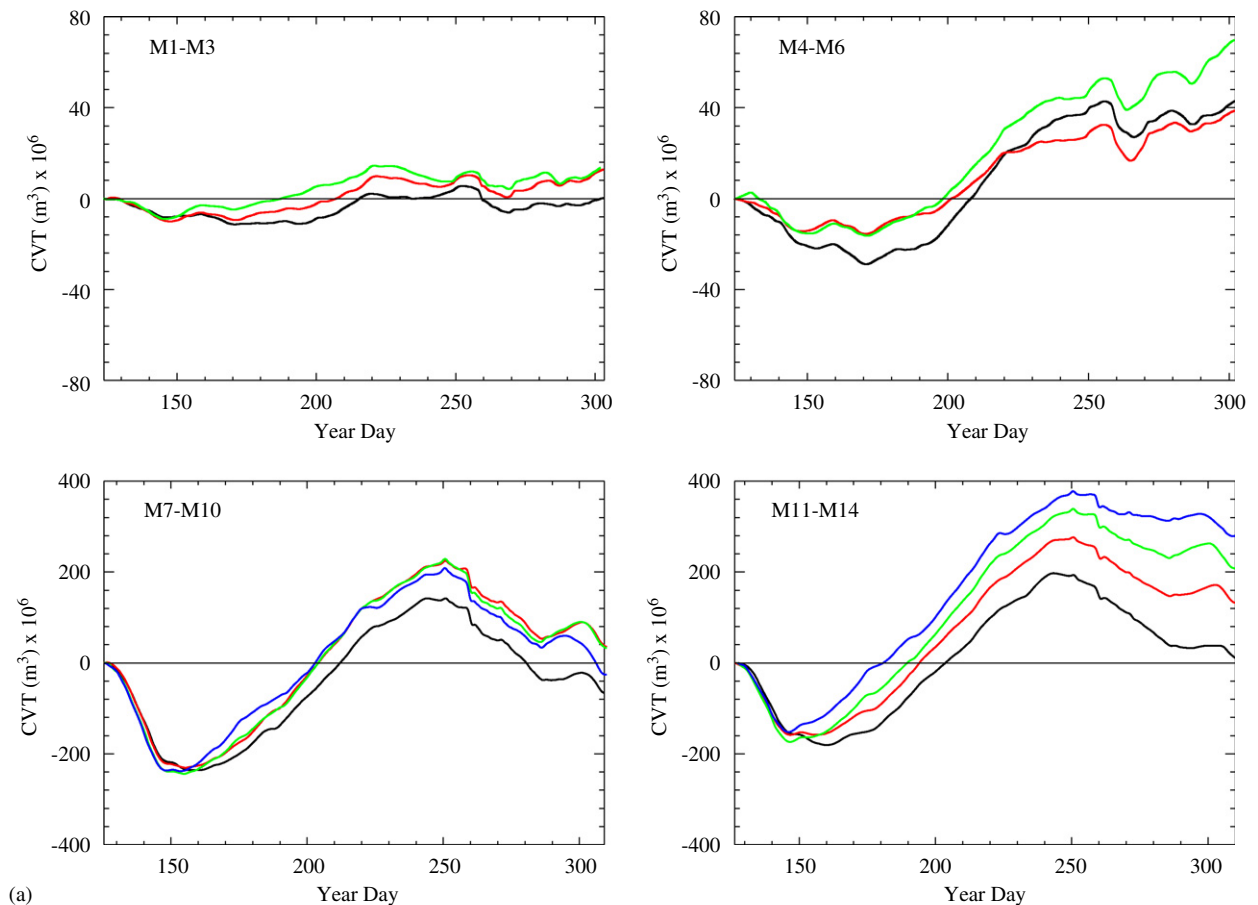


Fig. 7. Cumulative volume transported (CVT) per unit width versus time is shown for the measurement period. CVT is formed by integrating the depth-averaged velocities from the beginning of the measurement period up to each time in the measurement period and multiplying by the water depth for M1–M10 (L1–L3) and by 500 m for M11–M14 (L4): (a) along-shelf component (u); (b) cross-shelf component (v).

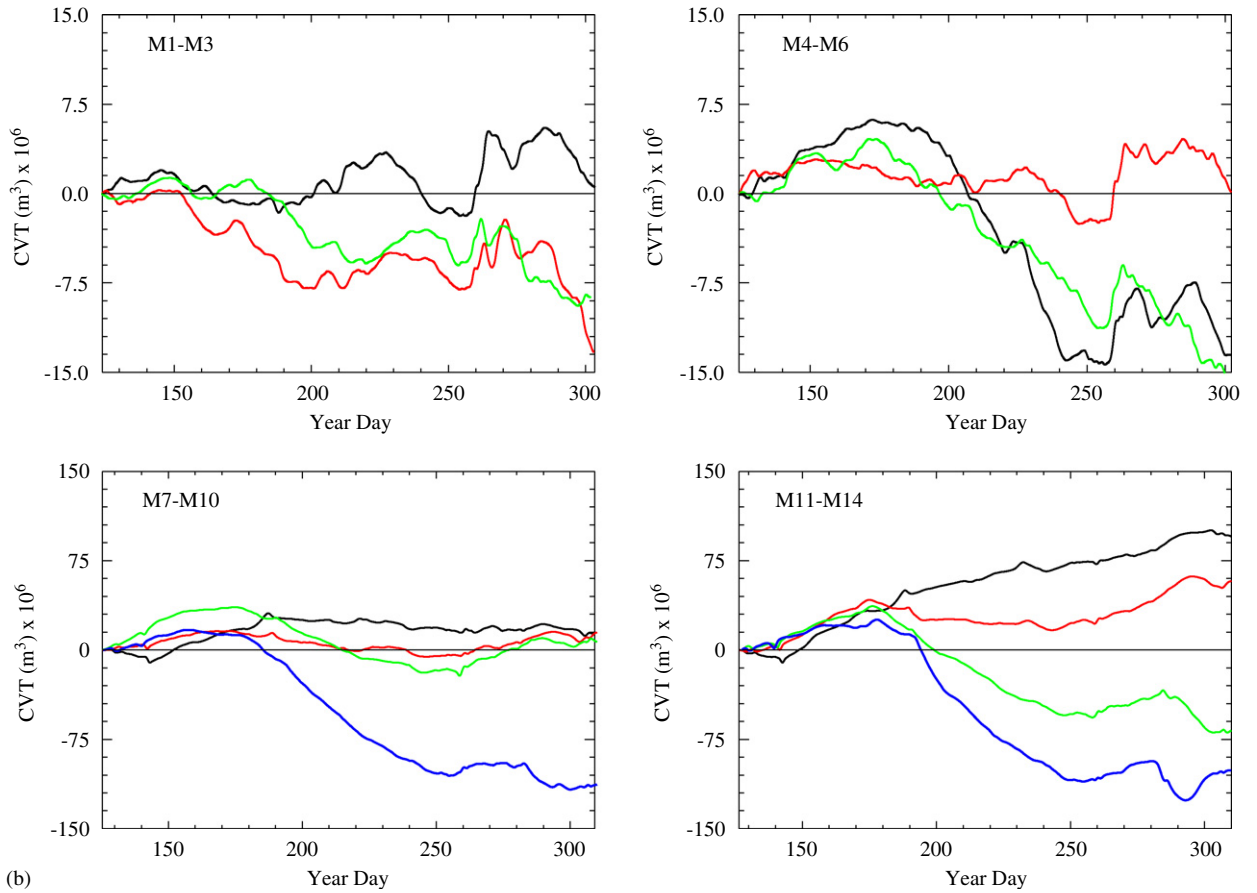


Fig. 7. (Continued)

time of integration, particularly in the deeper water along the slope (L3 and L4).

5. Depth-dependent currents

The degree of depth dependence can be quantified from the velocity profiles as follows. The velocity time series for the u (and similarly for v) component, a function of both depth (z) and time (t), consists of barotropic (u_{bt}) and depth-dependent (u_{dd}) parts and is given by

$$u(z, t) = u_{bt}(t) + u_{dd}(z, t). \quad (1)$$

The depth averaged or barotropic velocity time series is formed by:

$$u_{bt}(t) = \frac{1}{Z} \int_{z_1}^{z_2} u(z, t) dz, \quad (2)$$

where $Z = z_2 - z_1$, and z_1 and z_2 would ideally be the surface and bottom depths,

respectively, but here are the measured velocities at the top and bottom of the profiles (Table 1). The time anomaly of velocity can be expressed as

$$u'(z, t) = u(z, t) - \bar{u}(z), \quad (3)$$

where

$$\bar{u}(z) = \frac{1}{T} \int_0^T u(z, t) dt, \quad (4)$$

and T is the time duration of the data. Similarly, the time anomaly of the depth-dependent component of velocity consists of

$$u'_{dd}(z, t) = u_{dd}(z, t) - \bar{u}_{dd}(z), \quad (5)$$

where the time-mean of the depth-dependent component of velocity is given by

$$\bar{u}_{dd}(z) = \frac{1}{T} \int_0^T u_{dd}(z, t) dt. \quad (6)$$

The variance of the depth dependent component of velocity is

$$\overline{u'^2_{dd}}(z) = \frac{1}{T} \int_0^T u'^2_{dd}(z, t) dt \quad (7)$$

and the total velocity variance is

$$\overline{u'^2}(z) = \frac{1}{T} \int_0^T u'^2(z, t) dt. \quad (8)$$

The ratio of the mean depth-dependent EKE to the total EKE is

$$R_{eke}(z) = \frac{\overline{u'^2_{dd}}(z) + \overline{v'^2_{dd}}(z)}{\overline{u'^2}(z) + \overline{v'^2}(z)}. \quad (9)$$

Profiles of R_{eke} are shown for the entire time period for each mooring site in Fig. 8. The depth has been normalized for L1–L4 by the depth of the deepest velocity bin which is approximately the water depth for L1–L3 and 500 m for L4. These profiles show the relative contribution of the depth-dependent mean EKE to the total mean EKE. The overall average R_{eke} is 0.13, which implies that EKE from barotropic processes accounted for about 87% of the energy. If tides and higher frequency motions are included, the ratio increases to 0.17 and barotropic processes account for about 83% of the energy. The shape of R_{eke} is “C” shaped for all of the moorings. It can be characterized, from on the shelf at 60 m depth to down the slope at water depths of 1000 m, by three

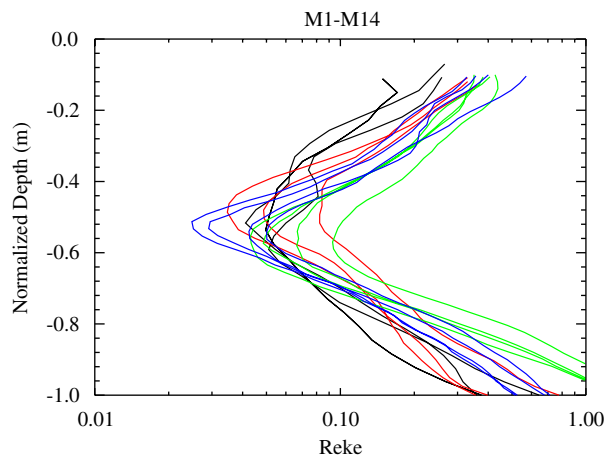


Fig. 8. Ratios of the time mean over the entire measurements period of depth-dependent eddy kinetic energy to the total eddy kinetic energy are shown for all the moorings along each line. Black, red, green, and blue colors correspond to moorings along lines 1–4, respectively. Depths have been normalized by the maximum depth of each velocity profile. R_{eke} magnitudes are given in a log scale on the x axis.

layers corresponding to a top layer encompassing approximately the upper 48%, the middle 12%, and the bottom 40% of the water column, respectively. EKE was almost entirely barotropic in the middle layer. Largest values of R_{eke} occurred at density gradients in the bottom layer that likely corresponded to cross-shelf exchanges and strong velocity shears. Large values in the top layer are associated with the top of the thermocline.

6. Wind driven circulation

The convergence of the wind stress curl is believed to be a primary forcing mechanism of the mean circulation in the Gulf of Mexico beyond the influence of the Loop Current, rings, and eddies (Sturges, 1993). Some studies have indicated that winds are important as a forcing mechanism only for the inner-shelf circulation (Cochrane and Kelly, 1986; Morey et al., 2005) and less important offshore. The wind pattern over the northern Gulf displays seasonal fluctuations (Gutierrez de Velasco and Winant, 1996; Wang et al., 1998), and during most of a typical year, i.e., September through May, the winds are generally easterly. Dominant synoptic scale disturbances, common for these months, are cold fronts with a frequency of 3–10 days. The summer months are usually characterized by weak southerly or southeasterly winds associated with the Bermuda high pressure system (Crout et al., 1984). During this season, sea-breeze forcing exists, and squalls, tropical storms, and hurricanes may aperiodically impact the region.

The origin of the eastward flow on the outer shelf near the shelf break in the eastern Gulf of Mexico is not well understood. In the western Gulf, the wind stress curl has been shown to drive the boundary currents (Sturges, 1993). Along-shelf winds were found to be highly correlated with along-shelf currents for regions west of 92.5° (Cochrane and Kelly, 1986) but found to be poorly correlated with along-shelf currents to the east (Chuang and Wiseman, 1983). The poor correlation was attributed to canyon intrusions and buoyancy processes.

There are a number of meteorological buoys located along the coast and offshore in the northern Gulf of Mexico, operated by the National Oceanic and Atmospheric Administration (NOAA) Data Buoy Center (NDBC), from which directly measured local and remote winds were obtained. One of these buoys (NDBC Station 42040 at 29.18°N, 88.21°W, Fig. 1) is located within our mooring array on the western side. Additional wind measurements

used for analyses were acquired from NDBC Station 42020 (26.94°N, 96.70°W) located near the Texas coast, NDBC Station 42002 (25.17°N, 94.42°W) located in the western Gulf, and the Coastal-Marine Automated Network (C-MAN) Station DPIA1 (30.25°N, 88.07°W) located on Dauphin Island, Alabama. The winds measured at buoys near the Texas coast and in the western Gulf are considered as representative of the remote wind forcing, while winds measured at buoys within our array and at Dauphin Island are considered as representative of a local wind forcing. Model-wind velocity components at 10 m elevation with 27 km horizontal resolution were extracted from the Coupled Ocean/Atmosphere Mesoscale Prediction System (COAMPS) (Hodur, 1997; Hodur and Doyle, 1999). Model and observed wind components were converted to wind stresses estimated according to the algorithm described by Large and Pond (1981). Additionally, winds stress curl was computed from the COAMPS data (not computed from the buoy data). Complex correlations between wind stress, wind stress curl, and depth averaged currents were also calculated. The correlations larger than 0.3 are considered statistically significant.

The vertically averaged currents at 90, 500 and 1000 m water depth (L2, L3, and L4) are well correlated with the local wind stress (0.65–0.89) and local wind stress curl (0.50–0.94) averaged over the moorings in May 2004 (P1), a period when winds are generally coherent over the northern Gulf of Mexico so there is little distinction between local and remote wind forcing. However, during the same time period, the currents on the shelf, at 60 m show much weaker relationship with the same wind stress (correlation below 0.60) and curl (correlation below 0.41). There is also very little correlation between the currents on the shelf (L1, L2) and the wind forcing in June through August 2004 (time periods P2 and P3). At the same time higher correlations are observed between the slope currents (L3, L4) and local wind stress curl (0.71–0.91) in P2. The currents on the slope also seem to respond well to fluctuations of the remote wind stress (correlations between 0.80 and 0.81) and wind stress curl (correlations between 0.75 and 0.82) in July and August 2004 (P3). Finally, high correlations (0.71–0.90) are found between the local wind stress curl and currents at all of the moorings on the shelf and slope during September and October 2004 (P4), a period when winds over the northern Gulf are

generally incoherent. Overall, the deeper currents at 90 m water depth on the shelf and down the slope at water depths of 500 and 1000 m respond more favorably to the wind stress curl than the shallower currents at 60 m water depth.

7. EOF analysis

The large-scale features of the combined shelf and slope flow are investigated using EOF analysis of the currents. The larger scale correlated modes of motion over the entire shelf and slope region covered by the mooring array are extracted in order to provide a simple picture of the dominant variability. Some important modes found only on the slope or only on the shelf were excluded from this type of analysis if their variances, compared to the dominant modes, are too small. A more complete analysis, not attempted here, would also focus separately on the shelf and slope modes. The EOF analysis was performed on the time anomalies of the combined vertically averaged currents, u'_{bt} and v'_{bt} , from all 14 moorings. Each u and v time series (low-pass filtered with a 40-h cutoff frequency) was interpolated to 6-h intervals and demeaned over the 170-day period from May 9, 2004 to October 26, 2004. The currents were not rotated for the EOF analyses. The individual vertically averaged time series were not normalized by their standard deviations, as is often recommended (Preisendorfer, 1988), because of the small range (6.8–9.7 cm/s) in the standard deviation of the speeds among the moorings. This allows the convention to be used in which the EOFs are normalized and non-dimensionalized, and units (m/s) are carried in the eigenvalues. This approach permits the eigenvectors to be interpreted directly since their relative magnitudes are maintained without rescaling with their individual standard deviations. The first two EOF modes account for 68.4% and 14.5% (combined 82.9%) of the total data set variance, and only the first two modes were resolved from surrounding modes according to the rule of thumb suggested by North et al., 1982. In addition, just the first two modes were found to be statistically significant according to the Monte Carlo approach of Overland and Preisendorfer (1982).

The mean vertically averaged currents and the first two EOF modes are displayed in Fig. 9 as vectors projecting from each mooring location on a regional map. The mean current (Fig. 9a) is

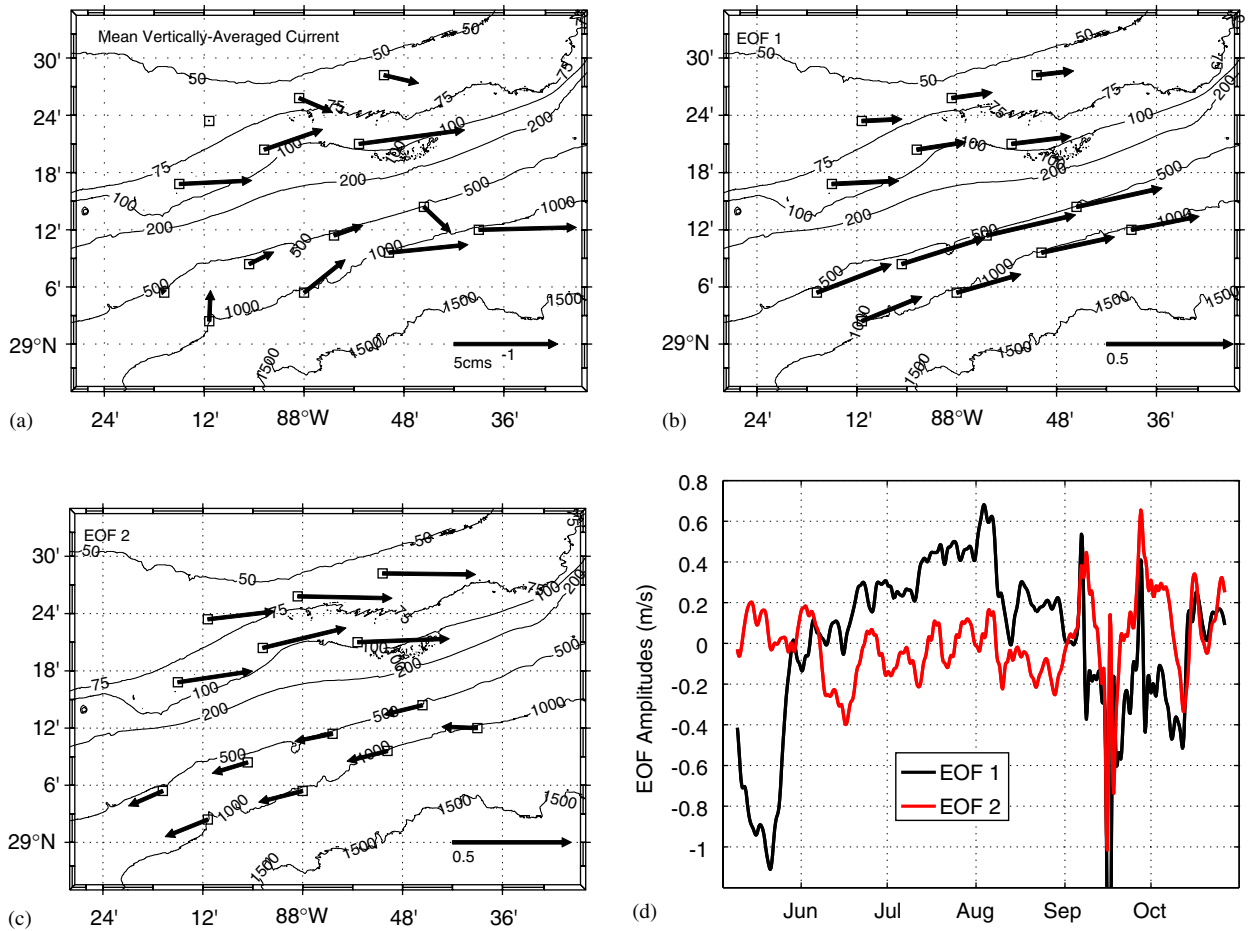


Fig. 9. (a) Mean vertically-averaged currents for May–October, 2004; (b) normalized vectors from the first EOF mode; (c) normalized vectors from the second EOF mode; (d) amplitude versus time for the first two EOF modes.

generally eastward, directed along isobaths, with speeds ranging from near zero at M1 to 5.1 cm/s at M6 on the shelf, and from near zero at M7 to 4.7 cm/s at M14 on the slope. The most energetic mode (EOF 1) (Fig. 9b) shows both the shelf and slope flows aligned in the same direction, approximately along isobaths, and that the flows reverse direction in unison as the EOF amplitude (Fig. 9d) changes sign. The average of normalized speeds on the shelf (moorings M1 through M6) is smaller (0.19) than the average normalized speed over the slope (0.31) despite the fact that the average velocities for the slope moorings did not include expected higher velocities in the upper 50 m while including velocities to approximately 500 m depth. In EOF 2, the vectors are again aligned along isobaths, but the shelf vectors are directed opposite to those on the slope (Fig. 9c). Also, in EOF 2,

opposite of results from EOF 1, the average speed on the shelf (0.34) is more than twice that over the slope (0.19). The amplitude versus time for the first two EOF modes is shown in Fig. 9d. The actual current speeds are achieved by multiplying the amplitude (which carries the units) by the normalized EOF vectors. The amplitudes of the first mode began in May with large negative values peaking near -1.1 m/s, which when multiplied by the first EOF vectors in Fig. 9b, produces a westward current with maximum average speeds near 29 cm/s on the shelf and 39 cm/s over the slope (not including the mean or other EOF modes). During the next three months, the EOF 1 amplitude is nearly always positive and reaches a maximum in the first days of August near 0.68 m/s, producing EOF 1 maximum eastward currents averaging 18 cm/s on the shelf and 24 cm/s on the slope.

During September and the first half of October the amplitudes of the first mode are again negative, producing westward currents, but punctuated by short periods of eastward currents as hurricanes passed through. The amplitudes of the second mode (primarily fluctuated around zero) are smaller than the first mode (variance of second mode was only 21% of the first mode variance) and are dominated by variability with periods from about 10 days to two weeks.

The vertically averaged velocities at all moorings are exactly correlated within each mode and the fluctuations within each mode occur independent of every other mode. The variability of the most significant modes should have some clear relationship to some physical phenomena, particularly when they represent such a large fraction of the total variance. As previously discussed, the vertically average currents show varying degrees of correlation to the wind stress or wind stress curl depending upon time period and mooring location. Overall, highest correlations are found over the slope. Comparison of time series of wind stress and EOF 1 amplitudes reveals another possible relationship at long time scales. The winds are shown as a progressive vector plot in Fig. 10. At the beginning of the observation period, the currents were directed downcoast when the winds were towards the northwest

(May 9). When the winds shifted toward the north (May 21), the along-shore currents rapidly accelerated upcoast changing the current direction from downcoast to upcoast. The along-shore currents then continued to accelerate upcoast more slowly in June and July as the winds continued northward. Acceleration of the currents ceased as the winds became variable and generally eastward (beginning July 11). Subsequently, the currents accelerated downcoast when the winds were directed southward or westward (beginning August 12), changing the current direction to downcoast. A possible relationship is suggested between the change in the currents and time integral of the wind stress. To examine this connection more closely, the time series of the amplitudes of the first two EOF amplitudes are plotted in Fig. 11 together with the integrals of the wind stress:

$$I_{\tau_x}(t) = \int_{t_0}^t \tau_x(t') dt', \quad (10)$$

$$I_{\tau_y}(t) = \int_{t_0}^t \tau_y(t') dt', \quad (11)$$

where τ_x and τ_y are the surface wind stress components in the east–west and north–south directions, respectively, measured at NDBC Station

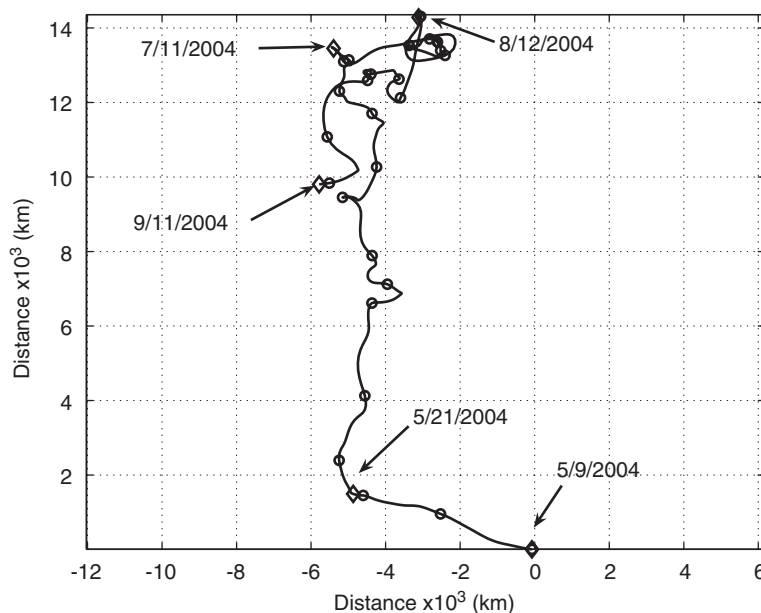


Fig. 10. Progressive vector diagram for the wind field obtained from NDBC buoy 42040. The buoy measurements were disabled by Hurricane Ivan in mid-September. Circle symbols are five days apart. Dates of major wind shifts in direction are marked by diamonds.

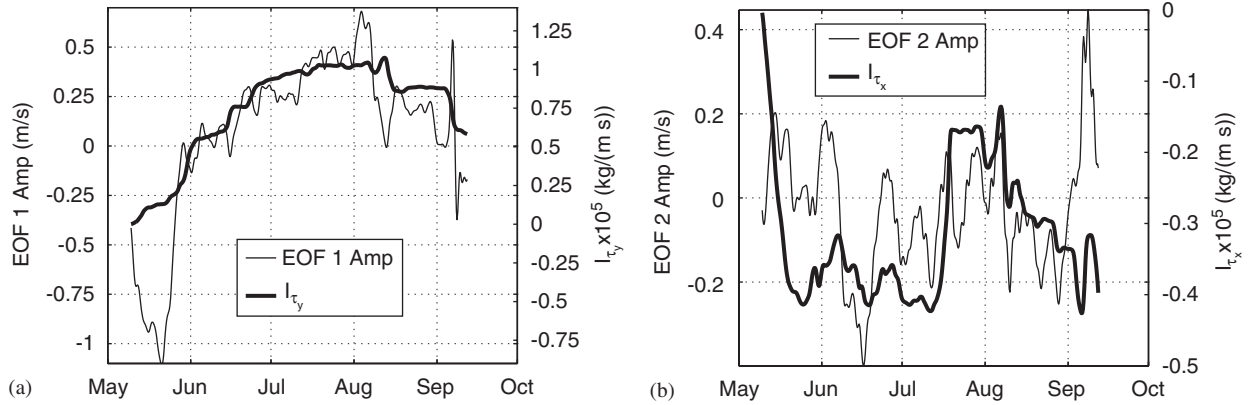


Fig. 11. (a) First mode EOF amplitude overlaid with the north–south component of the integrated wind stress (I_{τ_y}); (b) second mode EOF amplitude overlaid with the east–west component of the integrated wind stress (I_{τ_x}).

42040 (Fig. 1, between moorings M4 and M7), and t_0 is the time at the beginning of the time series. In Fig. 11a, the amplitude of EOF 1 is plotted with I_{τ_y} , showing a close correspondence between the longer-period trends of the two series. In Fig. 11b the time series of the EOF 2 amplitude is displayed with I_{τ_x} . In this case, the shorter-term (10 days to 2 weeks) fluctuations in the two series sometimes agreed. The large shifts in I_{τ_x} at the middle of May and July appear to correspond to similar displacements in the EOF 1 amplitude shown in Fig. 11a. While the amplitudes of both EOFs may be related to both components of the integrated wind stress, the longer-period fluctuations dominated EOF 1 and the shorter-term fluctuations dominated EOF 2. Multivariate linear regression for each EOF amplitude as a function of both components of the integrated wind stress indicates that only the long-term trends in both modes are directly predictable from the local integrated wind stress. In addition, the changes of vertically averaged velocity computed from the first EOF appears to be consistent with the magnitude of changes in I_{τ_y} . The barotropic forced response of shelf and slope currents to a suddenly applied uniform wind stress was studied by Csanady (1974). The particular case having onshore winds, bottom friction, and a composite bottom topography including shelf, slope, and deep ocean was not studied. Here, the relative magnitudes of two terms from the depth-averaged equations of motion (Csanady, 1974) integrated over time are assessed

$$\int_{t_0}^t \frac{\partial u(t')}{\partial t'} dt' = u(t) - u(t_0) \quad (12)$$

and

$$\int_{t_0}^t \frac{\tau_y(t')}{\rho_0 H} dt' = \frac{I_{\tau_y}(t)}{\rho_0 H}, \quad (13)$$

where ρ_0 is a reference density (1027 kg/m^3) and H is the water depth. In Eq. (12), the integrated acceleration is the change in the east–west component of momentum, and Eq. (13) is the momentum added through surface stress from the north–south component of the wind. From the beginning of the series to the beginning of August, I_{τ_y} increased from zero to about 10^5 kg/(ms) while the amplitude of EOF 1 increased from about -0.4 to 0.4 m/s . At mooring M8 over the slope, $H = 500 \text{ m}$ and the magnitude of the u and v eigenvectors for mode 1 was about 0.34. Therefore, $u - u_{t_0} = 0.27 \text{ m/s}$ and $I_{\tau_y}/(\rho_0 H) = 0.19 \text{ m/s}$, forming a reasonable agreement between the two. As H decreases northward onto the shelf, the vertically integrated velocity should increase. As discussed previously, the speeds predicted on the shelf from EOF 1 are about $\frac{2}{3}$ of those on the slope, but the depths are less than $\frac{1}{5}$ of those on the slope. For example at mooring M1, $H = 60 \text{ m}$, $u - u_{t_0} = 0.13 \text{ m/s}$ and $I_{\tau_y}/(\rho_0 H) = 1.6 \text{ m/s}$. These two terms are nearly equal over the slope, but are nearly an order of magnitude different over the shelf. A more complete analysis exploring the relationships between the vertically averaged currents and the wind stress, incorporating simple models of the shelf and slope currents is called for but is beyond the scope of this paper.

The first two EOF modes account for 82.6% of the vertically-averaged velocity variance of the combined 14 moorings. The distribution of the

explained variance among the moorings on the shelf and slope is shown in Fig. 12. For each mooring, the time series of the temporal anomalies of the velocity components, $\hat{u}'_{bt}(t)$ and $\hat{v}'_{bt}(t)$ are generated from the first two EOF eigenvectors and amplitudes. The percent of the variance explained by the first two EOFs at each mooring for u , v , and combined u and v components, are given by

$$V_u = 100 \left[1 - \frac{\int_{t_0}^{t_0+T} (u'_{bt}(t) - \hat{u}'_{bt}(t))^2 dt}{\int_{t_0}^{t_0+T} (u'_{bt}(t))^2 dt} \right], \quad (14)$$

$$V_v = 100 \left[1 - \frac{\int_{t_0}^{t_0+T} (v'_{bt}(t) - \hat{v}'_{bt}(t))^2 dt}{\int_{t_0}^{t_0+T} (v'_{bt}(t))^2 dt} \right] \quad (15)$$

$$V_{u+v} = 100 \left[1 - \frac{\int_{t_0}^{t_0+T} (u'_{bt}(t) - \hat{u}'_{bt}(t))^2 dt + \int_{t_0}^{t_0+T} (v'_{bt}(t) - \hat{v}'_{bt}(t))^2 dt}{\int_{t_0}^{t_0+T} (u'_{bt}(t))^2 dt + \int_{t_0}^{t_0+T} (v'_{bt}(t))^2 dt} \right] \quad (16)$$

and are written at the upper left, upper right and below each mooring location. A large percentage of the east–west velocity was reproduced by the EOFs (V_u ranges from 89% to 98% for the slope moorings and 73–83% for the shelf moorings). However, only a small percentage of the north–south variance (1–21%) is explained at the shelf

moorings. Even at the slope moorings, V_v decreases toward the east, ranging from 89% down to 24%. The low percentage of cross-shelf variance explained by the EOFs can be attributed to both small cross-shelf and along-shelf correlation length scales for the cross-shelf velocity, particularly near the DeSoto Canyon.

8. Discussion

Previous observations of currents along the northern Gulf of Mexico coast have found that the flow is usually towards the east (Hamilton et al., 2000; He and Weisberg, 2002; Hsueh and Golubev, 2002; Wang et al., 2003) and that wind stress is the dominant mechanism for driving the circulation

over the shelf (Morey et al., 2003). During May–October, 2004, currents on the shelf were variable and the mean currents generally followed the bathymetry, while currents on the slope were highly steered by the bathymetry. Flow was predominately along shelf although small sporadic cross-shelf flows did occur. The currents at each

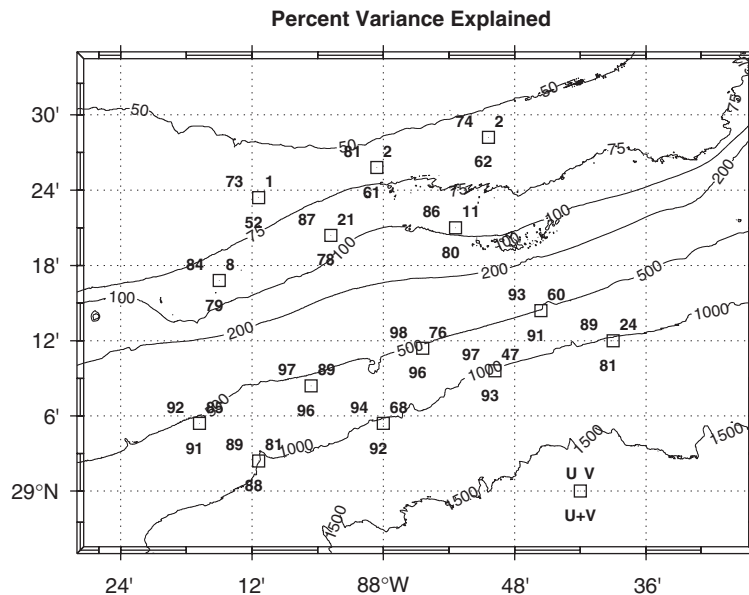


Fig. 12. (a) Distribution of the explained variances at each of the moorings from the first two EOF modes is shown. The variances, which are displayed at the upper left and upper right, and below each mooring position, correspond to the east–west variance, north–south variance, and combined variance, respectively.

mooring over the six-month measurement period contained several current reversals, and thus the average currents were just a few cm/s. Therefore, the measurement period was divided into four time periods based on the dominant flow directions.

Flow was predominantly downcoast (westward) during P1 and P4 and opposite the usual eastward flow. Our results indicate that at least some of the westward flow can be attributed to the integrated wind stress which correlated very favorably with the amplitudes of the first mode EOF of the shelf/slope barotropic current field. In addition, examination of model results from NRL's Intra-Americas Sea Ocean Nowcast/Forecast System (IASNFS) (Ko et al., 2003) and Sea-surface heights (SSHs) from satellite observations revealed that during May 2004, the Loop Current extended to almost 28°N and a Loop Current ring existed in the western Gulf with a pair of cyclones trailing the ring. The northeastern cyclone (about 100 km in diameter) impinged on the SEED moorings. Our analyses suggest that the westward currents at our moorings are driven at least partly by wind and partly by the cyclonic eddy during P1. Similarly, during P4, flow was also towards the west. Analysis of model output and satellite imagery revealed that a Loop Current Ring separated in August 2004 and an associated cyclonic eddy formed in September, after Hurricane Ivan that could have reversed the eastward flow on the shelf/slope. The cyclonic eddy was about 70 km in diameter, and appeared to directly affect the currents on the slope, and to indirectly affect the currents on both the shelf and slope through smaller anticyclonic eddies (30–50 km in diameter), perhaps generated by the cyclone from instability mechanisms. In addition, part of the variability during P4 is attributed to Hurricane Francis (Day 249) and Hurricane Ivan (Day 259). Velocity maxima associated with these storms are seen in the velocity contour sections (Fig. 2) and depth-averaged velocity time series (Fig. 6).

Currents reversed directions (from west to east) during June 2004 (P2) which is considered here as a transition period. The currents on the shelf were not directly wind driven since their correlations with the winds were low. Hence, these currents were likely controlled by other forcing mechanisms such as baroclinic and/or barotropic pressure gradients, while on the slope they may have been part of the cyclonic eddy field as well as could have been driven by the wind stress curl. During July through August (P3), the prevalent eastward flow conditions

returned. Eddy activity was not indicated by SSH images. This fairly strong eastward flow in July and August 2004 could have been then an extension of the eastward flow present throughout the year along the shelf break in the northwestern Gulf of Mexico (Nowlin et al., 1998). Analyses here suggest that the long-period eastward flow can be at least partly explained by the build-up of the integrated north–south wind stress. In addition, flow at the shelf break (L2) and on the slope (L3 and L4) was correlated with the remote wind stress curl off Texas. Cross-shelf flows during this time period were likely the result of baroclinic pressure gradients originating from upwelling and other processes associated with the DeSoto Canyon. Current variability was highest, particularly on the shelf on L1 and L2, from mid-September to early November (P4) (end of the measurement period). Mean flow on the slope during P4 was westward but the mean flows were not significant since the mean vectors were within their respective standard deviation ellipses (Fig. 4). Currents on both the shelf and slope during P4 were highly correlated with the local wind stress curl. However, SSH images indicated the presence of eddies which could also influence the current field.

Cross-shelf transports were much smaller than the along-shelf transports. Some cross-shelf transports were induced by impinging cyclonic eddies. Onshore and offshore flows and associated transports were often found when the circulation is dominated by downcoast and upcoast flows, respectively. Periods of onshore flows appeared to be associated with flow reversals towards the east and offshore flows appeared to be associated with flow reversals towards the west, consistent with Coriolis forcing (Fig. 5). There does not appear to be a preferred mean current direction along the slope that is always associated with onshore or offshore flows. Deep flows at 900 m were largest and similar to flows at 500 m during the eddy influenced periods (P1 and P4) and were almost negligible when wind-driven upcoast flows prevailed (P3). Storms, such as Hurricanes Ivan and Francis had relatively little impact on the transports (Fig. 7).

Tongues of low salinity and similar patterns of chlorophyll concentration have been observed extending southeastward from the DeSoto Canyon along the eastern edge of the Loop Current (Morey et al., 2005). Work by Morey et al. (2003) suggested that the edge of the DeSoto Canyon is a pathway for cross-shelf exchange. They suggested that

surface water properties of the northeastern Gulf of Mexico may be controlled by a combination of wind-driven shelf circulation and eddy interactions. Our measurements suggest that the preferred location for offshore flow was on the eastern side of the array, located about 50 km from the western side of the DeSoto Canyon. Onshore flow was observed on the western side of the array.

Along-shore pressure gradients have been thought to be important in controlling the regional flow patterns on the western Louisiana shelf (Crout, 1983; Wiseman et al., 1992). These studies have not been definitive due to the lack of suitable observations. Interestingly, Rouse et al. (2005) applied an existing vertically integrated, non-linear numerical model forced by monthly mean wind fields and found that the dominant balance of forces in the model was between the Coriolis forces, pressure gradients, and wind stresses. Walker et al. (2001) also found weak coherences with the along-shore pressure gradients and inner shelf currents over the West Louisiana shelf. The source of the pressure gradient was not known but was thought to be dominated by sea surface slope. The EOF analysis performed here suggests that the integral of the north–south component of the wind stress is important in determining the pressure gradient over the shelf which is a major factor in determining the long-period eastward or westward flow patterns. Shorter period variability in both east–west and north–south directions is related to the integrated east–west component of the wind stress. Cyclonic eddies are also thought to contribute to current patterns.

9. Conclusions

Currents in the SEED region are found to be energetic and speeds in excess of 30 cm/s were common. Time scales of along-shelf flows were typically about a week while time scales of along-slope flows were generally a month or more. Time scales of cross-shelf flows on both the shelf and slope were shorter, generally ranging from a couple of days to a week. Currents on the shelf and slope in the SEED region were strongly steered by the bathymetry. On the slope, currents strongly followed the bathymetric contours and generally were eastward but reversals to the west were observed. On the shelf, currents were more variable than on the slope but tended to parallel the currents on the slope. Flow was dominant in the along-shelf

direction. Subsurface current maximums were common. Onshore (offshore) flow pulses occurred when the currents changed direction from downcoast to upcoast (upcoast to downcoast). There was a tendency for onshore flow on the western side of the moorings and offshore flow on the eastern side of the slope moorings. The offshore flow may have been related to deep ocean processes in the nearby deep DeSoto Canyon where cyclones and anticyclones can intrude. Currents were highly barotropic outside of the near-surface and bottom current layers. Barotropic processes accounted for about 80% of the EKE.

Several factors had a major impact on the currents during the SEED measurement period. Both local winds and remote winds were factors in the circulation. The first two EOF modes accounted for 83% of the total variance of the barotropic currents. The dominant modes of variability appeared to be strongly related to the integrated wind stress. Longer-period fluctuations (EOF 1) were largely determined by the integral of the north–south wind stress while the shorter-period fluctuations (EOF 2) were influenced by the integral of the east–west wind stress. The acceleration term nearly balanced the surface wind stress term in the momentum equation on the slope at long time scales. The direction of the long-term barotropic general east–west flow across the moorings was determined by the integral of the north–south component of the wind stress. Currents were accelerated eastward when the winds were towards the north and accelerated westward when the winds were towards the west and south. Less commonly, cyclonic eddies associated with the Loop Current or Loop Current rings impacted the flow patterns and may have forced some westward flow. Smaller anticyclonic eddies associated with cyclonic eddies increased the current variability on the shelf and slope. The eddies apparently had no seasonal pattern but the exchange processes induced by these eddies could be affected by the variability of the shelf circulation. However, cross-shelf transports associated with non-eddy periods were comparable to cross-shelf transports that occurred during eddy periods. Often, offshore transports were associated with upcoast or eastward currents and onshore transports were associated with downcoast or westward currents. There was not a preferred long-term current direction along the slope that was always associated with either onshore or offshore flows. Storms such as Hurricane Ivan

caused short-term large current variability that had relatively small effects on the total cross- and along-shelf transports during the observation period.

Acknowledgments

This work was supported by the Office of Naval Research as part of the NRL's basic research project "Slope to Shelf Energetics and Exchange Dynamics (SEED)" under program element 0601153N (NRL-Stennis Space Center contribution no. NRL/JA/7330-05-5325).

References

- Chassignet, E.P., Hurlburt, H.E., Smedstad, O.M., Halliwell, G.R., Hogan, P.J., Wallcraft, A.J., Baraille, R., Bleck, R., 2006. The HYCOM (Hybrid Coordinate Ocean Model) data assimilative system. *Journal of Marine Systems*, in press.
- Chuang, W., Wiseman Jr., W.J., 1983. Coastal sea level response to frontal passages on the Louisiana-Texas shelf. *Journal of Geophysical Research* 88, 2615–2620.
- Cochrane, J.D., Kelly, F.J., 1986. Low-frequency circulation on the Texas-Louisiana shelf. *Journal of Geophysical Research* 91, 10,645–10,659.
- Crout, R.L., 1983. Wind-driven, near-bottom currents over the west Louisiana inner shelf, Ph.D. Dissertation, Louisiana State University, Baton Rouge, LA., 117pp.
- Crout, R.L., Wiseman Jr., W.J., Chuang, W.S., 1984. Variability of wind driven currents, west Louisiana inner continental shelf: 1978–1979. *Contributions in Marine Science* 27, 1–11.
- Csanady, G.T., 1974. Barotropic currents over the continental shelf. *Journal of Physical Oceanography* 4, 357–371.
- Ford, J., Wayland, R., Waddell, E., Hamilton, B., 1988. Meteorological Database and Synthesis for the Gulf of Mexico, OCS Study, MMS 88-0064, U.S. Dept of the Interior, Mineral Management Service, New Orleans, LA, 486pp.
- Garwood, R.W., Fett, R., Rabe, K., Brandli, H., 1981. Ocean frontal formation due to shallow water cooling effects as observed by satellite and simulated by a numerical model. *Journal of Geophysical Research* 86, 11000–11012.
- Gutierrez de Velasco, G., Winant, C.D., 1996. Seasonal patterns of wind stress and wind stress curl over the Gulf of Mexico. *Journal of Geophysical Research* 101, 18,127–18,140.
- Hamilton, P., 1990. Deep current in the Gulf of Mexico. *Journal of Physical Oceanography* 20, 1087–1104.
- Hamilton, P., Berger, T.J., Singer, J.J., Waddell, E., Churchill, J.H., Leben, R.R., Lee, T.N., Sturges, W., 2000. Desoto Canyon Eddy Intrusion Study, Final Report, Volume II: Technical Report, OSC Study MMS 2000-080, U.S. Department of the Interior, Mineral Management Service, Gulf of Mexico OCS Region, New Orleans, LA, 275pp.
- Hamilton, P., Berger, T.J., Johnson, W., 2002. On the structure and motions of cyclones in the northern Gulf of Mexico. *Journal of Geophysical Research* 107 (C12) Art. No. 3208.
- He, R., Weisberg, R.H., 2002. West Florida shelf circulation and temperature budget for the 1999 spring transition. *Continental Shelf Research* 22 (5), 719–748.
- Hodur, R., 1997. The Naval research laboratory coupled ocean/atmosphere mesoscale prediction system (COAMPS). *Monthly Weather Review* 125, 1414–1430.
- Hodur, R.M., Doyle, J.D., 1999. The Coupled Ocean/Atmosphere Mesoscale Prediction System (COAMPS). In: Mooers, C. (Ed.), *Coastal Ocean Prediction*. AGU, Washington, DC, pp. 125–155.
- Hogg, N.G., Siedler, G., Zenk, W., 1999. Circulation and variability at the southern boundary of the Brazil Basin. *Journal of Physical Oceanography* (29), 145–157.
- Hsueh, Y., Golubev, Y., 2002. A numerical model calculation of the flow in the DeSoto Canyon in response to northerly wind bursts in winter, In: Hsueh, Y., Weisberg, R. (Eds.), *North-eastern Gulf of Mexico Circulation Modeling Study: Draft Final Report*. US Department of the Interior, Minerals Management Service, Gulf of Mexico OCS Region, New Orleans, LA, pp. 25–51.
- Huh, O.K., Wiseman Jr., W.J., Rouse Jr., L.J., 1978. Winter cycle of sea surface thermal patterns, northeastern Gulf of Mexico. *Journal of Geophysical Research* 83, 4523–4529.
- Huh, O.K., Rouse, L.J., Walker, N.D., 1984. Cold air outbreaks over the Northwest Florida Continental Shelf: heat flux processes and hydrographic changes. *Journal of Geophysical Research* 89 (C1), 717–726.
- Ko, D.S., Preller, R.H., Martin, P.J., 2003. An experimental real-time intra Americas Sea Ocean nowcast/forecast system for coastal prediction, *Proceedings, AMS Fifth Conference on Coastal Atmospheric and Oceanic Prediction and Processes*.
- Large, W.G., Pond, S., 1981. Open ocean momentum flux measurements in moderate and strong winds. *Journal of Physical Oceanography* 11, 324–336.
- Mitchell, D.A., Teague, W.J., Jarosz, E., Wang, D.W., 2005. Observed currents over the outer continental shelf during Hurricane Ivan. *Geophysical Research Letters* V32, L11610.
- Morey, S.L., Martin, P.J., O'Brien, J.J., Wallcraft, A.A., Zavala-Hidalgo, J., 2003. Export pathways for river discharged fresh water in the northern Gulf of Mexico. *Journal of Geophysical Research* 108 (C10), 3303.
- Morey, S.L., Zavala-Hidalgo, J., O'Brien, J.J., 2005. The seasonal variability of continental shelf circulation in the northern and western Gulf of Mexico from a high-resolution numerical model. *New Developments in the Circulation of the Gulf of Mexico*, American Geophysical Union Monograph, submitted.
- North, G.R., Bell, T.L., Cahalan, R.F., 1982. Sampling errors in the estimation of empirical orthogonal functions. *Monthly Weather Review* 110, 699–706.
- Nowlin, W.D., Jr., Jochens, A.E., Reid, R.O., DiMarco, S.F., 1998. Texas–Louisiana Shelf circulation and transport processes study: Synthesis report, vol.1, Technical report, U.S. Department of the Interior, MMS, Gulf of Mexico OCS Region, New Orleans, LA., OCS Study MMS 98-0035, 502pp.
- Ohlmann, J.C., Niiler, P.P., Fox, C.A., Leben, R.R., 2001. Eddy energy and shelf interactions in the Gulf of Mexico. *Journal of Geophysical Research* 106, 2605–2620.
- Overland, J.E., Preisendorfer, R.W., 1982. A significance test for principal components applied to a cyclone climatology. *Monthly Weather Review* 110, 1–4.

- Paluszkiwicz, T., Atkinson, L.P., Posmentier, E.S., McClain, C.R., 1983. Observations of a Loop Current frontal eddy intrusion onto the west Florida shelf. *Journal of Geophysical Research* 88, 9639–9652.
- Perkins, H., deStrobel, F., Gualdesi, L., 2000. The Barny Sentinel Trawl-resistant ADCP bottom mount: design, testing, and application. *IEEE Journal Oceanic Engineering* V25 (4), 430–436.
- Preisendorfer, R.W., 1988. *Principal Component analysis in Meteorology and Oceanography*. Elsevier, 425pp.
- Rouse, L.J., Jr., Wiseman, W.J., Jr., Inoue, M., 2005. Aspects of the Louisiana Coastal Current, OCS Study MMS 2005-039, U.S. Department of the Interior, Minerals Management Service, Gulf of Mexico OCS Region, New Orleans, LA., 50pp.
- Sturges, W., 1993. The annual cycle of the western boundary current in the Gulf of Mexico. *Journal of Geophysical Research* 98, 18,053–18,068.
- Teague, W.J., Jarosz, E., Keen, T.R., Wang, D.W., Hulbert, M.S., 2006. Bottom scour observed under Hurricane Ivan. *Geophysical Research Letters* 33, L07607.
- Vidal, V.M.V., Vidal, F.V., Perezmolero, J.M., 1992. Collision of a Loop Current anticyclonic ring against the continental shelf slope of the western Gulf of Mexico. *Journal of Geophysical Research* 97, 2155–2172.
- Vukovich, F.M., 1988. Loop Current boundary variations. *Journal of Geophysical Research* 93, 15585–15591.
- Walker, N.D., Jarosz, E., Murray, S.P., 2001. An investigation of pressure and pressure gradients along the Louisiana/Texas inner shelf and their relationships to wind forcing and current variability, OCS Study MMS 2001-057, U.S. Department of the Interior, Minerals Management Service, Gulf of Mexico OCS Region, New Orleans, LA., 40pp.
- Wang, D., Oey, L., Ezer, T., Hamilton, P., 2003. Near-surface currents in DeSoto Canyon (1997–1999): comparison of current meters, satellite observation, and model simulation. *Journal of Physical Oceanography* 33 (1), 313–326.
- Wang, D.W., Mitchell, D.A., Teague, W.J., Jarosz, E., Hulbert, M.S., 2005. Extreme waves under Hurricane Ivan. *Science* 309, 896.
- Wang, W., Nowlin Jr., W.D., Reid, R.O., 1998. Analyzed surface meteorological fields over the northwestern Gulf of Mexico for 1992–1994: mean, seasonal and monthly patterns. *Monthly Weather Review* 126, 2864–2883.
- Wiseman, W.J., Jr., Bierman, V.J., Jr., Rabalais, N.N., Turner, R.E., 1992. Distribution and characteristics of hypoxia on the Louisiana shelf in 1990 and 1991. *Nutrient Enhanced Coastal Ocean Productivity*, TAMU-SG-92-109, Texas A&M University Sea Grant College Program, College Station, TX., 21–26.